Inverted Thickness Dependence of Thermal Transport in Nanocrystal Supercrystals Down to the Monolayer

Matias Feldman, Juan Barrios-Capuchino, Hervé Cruguel, Sébastien Royer, Claire Abadie, Danièle Fournier, Emmanuel Lhuillier, Jose Ordonez-Miranda, Emmanuelle Lacaze, Florian Schulz, et al.

Inverted Thickness Dependence of Thermal Transport in Nanocrystal Supercrystals Down to the Monolayer

*Matias Feldman, Juan J. Barrios-Capuchino, Hervé Cruguel, Sébastien Royer, Claire Abadie, Danièle Fournier, Emmanuel Lhuillier, Jose Ordonez-Miranda, Emmanuelle Lacaze, Florian Schulz, James K. Utterback**

M. Feldman, Dr. H. Cruguel, S. Royer, Dr. C. Abadie, Prof. D. Fournier, Dr. E. Lhuillier, Dr. J. Ordonez-Miranda, Dr. E. Lacaze, Dr. J. K. Utterback*

Sorbonne Université, CNRS, Institut des NanoSciences de Paris, 75005 Paris, France

*E-mail: james.utterback@sorbonne-universite.fr

J. J. Barrios-Capuchino, Dr. F. Schulz

Institute for Nanostructure and Solid State Physics, University of Hamburg, Luruper Chaussee 149, 22761 Hamburg, Germany

Keywords

nanoscale thermal transport, colloidal nanocrystals, supercrystal, thermoreflectance, spatiotemporal microscopy, ballistic phonon transport

Abstract

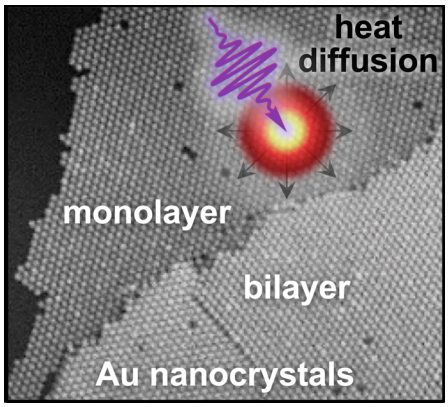

Understanding the thermal properties of nanocrystal solids is important for their implementation. However, probing the intrinsic properties of monolayer to few-layer supercrystals where non-diffusive effects can emerge has remained elusive. Here we use spatiotemporally-resolved thermoreflectance microscopy and correlative atomic force microscopy to locally access lateral thermal transport in gold nanocrystal supercrystals with long polymer ligands from the monolayer up to eight layers. In contrast to the thermal size effect of typical thin film materials, we demonstrate that above a few supercrystal layers the thermal diffusivity is nearly constant with increasing thickness. Notably, the mono-to-few layer range moreover experiences an inverted thickness dependence wherein the lateral thermal diffusivity increases when approaching the monolayer to a value 30–60% larger than the bulk. Simulations of quasi-ballistic thermal transport successfully model the experimental trend, indicating the need to account for the phonon mean free path in the ligand matrix and the geometry of scattering interfaces. Phonons responsible for heat transport within the nanocrystalline composite have mean free paths shorter than the thickness of single supercrystal layers. This leads to behavior distinct from typical thickness-dependent phonon–boundary scattering. These unusual behaviors present important considerations and opportunities for thermal management in applications of nanocrystal solids.

1. Introduction

Colloidal nanocrystal (NC) supercrystals (SCs) propose a tunable platform for bottom-up design of unique thermoelectric,[1–4] plasmonic,[5,6] nanoelectronic,[7] optoelectronic[8] and phononic[9] material properties. Very thin NC supercrystals and two-dimensional monolayers in particular hold interest for collective plasmonic coupling,[5,10] charge and spin transport,[11] optimization of LED recombination layers,[12] maximizing the gate effect in field-effect transistors,[13] catalysis,[14,15] and temperature and molecular sensing.[16] Nanoscale thermal management is critical for such applications as their operation inevitably generates or utilizes heat. Research over the past decade has shown that, in assemblies of nanostructures, thermal transport is a complex multiscale problem. There is a cascade of thermal transfer steps within nanomaterial units or interstitial media, across various interfaces,[17–21] transport across defects and microstructure,[22–25] and dissipation to the environment.[20,21] A key feature of three-dimensional NC assemblies is that their thermal transport is slow, being dominated by the ligands and phonon scattering at the NC–ligand interfaces with very little dependence on the core material.[17,18,22,26–28] From the perspective of polycrystalline materials, NC assemblies are effectively solids with well-defined nanograins.[26] These points lead to the central hypotheses of this paper: (1) the thermal transport properties of NC SCs should have an exceptionally weak dependence on film thickness (or the number of SC layers); (2) they may only reveal a breakdown of Fourier's law when approaching the scale of a single layer. Such behavior would be in contrast to many materials ranging from metallic films[29] and Si nanowires[30] to layered two-dimensional transition metal dichalcogenides[31] and supported graphene.[30] In those other materials, nanoscale thermal transport is characterized by the so-called thermal size effect wherein the thermal conductivity substantially decreases with decreasing size (i.e., sample thickness) when the finite size is below the heat carrier mean free path. Over the few to hundreds of nanometers range, this decrease is often down by 30–90% from the material's bulk thermal conductivity. An unconventional film thickness dependence of thermal conductivity would therefore be an important property in the design of colloidal NC-based systems. Thus, it is important to investigate the thermal properties of NC systems down to very thin assemblies where deviations from diffusive behavior might be expected.

Direct access to the intrinsic thermal transport properties of NC SCs down to mono-to-few layers is a challenge. It requires precise SC layer control with low defect density and a probe of heat flow with both spatial resolution below the SC grain size and dynamical information to separate the influence of the environment. Self-assembly protocols can achieve highly ordered mono-, bi-, and multi-layer NC SCs extending tens to hundreds of microns with few defects that are transferable to various substrates.[32,33] Despite this structure of such samples, fabricating thermal contacts in the appropriate locations relative to each desired region and distinguishing substrate effects would make traditional thermal measurements extremely difficult. However, the long-range order of such systems makes them amenable to local, optically-based thermal probes such as thermoreflectance.[34,35] Thermoreflectance has previously been applied to multilayer NC films and SCs to establish the role of the NC–ligand interface,[17,18] NC core diameter,[17,18] disordered NC films and NC SC ordering,[22,23] anisotropic thermal transport,[25] and thickness-dependent dissipation to the substrate.[20,36] The thermal conductivity for different film thicknesses was also measured, but in the multilayer regime.[17,18] However, in the case of monolayer NC SCs, using both a metallic transducer layer and substrate—as is typically done in thermoreflectance experiments—would necessitate modeling with many correlated parameters. While a transducer can be avoided by using NC core material with well-understood thermoreflectance signals such as Au NCs,[20,23,25] a substrate is important for NC film preparation. Thus, a clear separation of timescales is needed to access transport intrinsic to the SC. In particular, spatiotemporally-resolved thermoreflectance[23,25,36–39] is well suited to providing a local, dynamic probe of in-plane thermal transport without the use of models.

Here, we use spatiotemporally-resolved thermoreflectance to locally probe heat transport and relaxation in ordered SCs of colloidal Au NCs as a function of the number of layers from monolayer up to eight layers. We image lateral heat transport over hundreds of picoseconds to hundreds of nanoseconds with sub-micron resolution, allowing for the isolation of regions with a well-defined number of SC layers that each extend several microns. The thermal diffusivity is obtained directly through the lateral expansion of a heat pulse without relying on typical transducer-film-substrate multi-layer thermal transfer models. By reproducing the experiments in finite element simulations, we identify a separation of timescales between heat transfer from the NC core to the ligand medium, lateral transport through the SC between NCs, and transfer to the glass substrate. We find that for few-to-eight layers the lateral thermal diffusivity of the SC is constant as a function of the number of layers within error. Importantly, we reveal an inverted thermal size effect in the mono-to-few layer range wherein the lateral thermal diffusivity increases when approaching the monolayer to a value 30–60% larger than the bulk. Finite element simulations and effective medium approximation (EMA) calculations that assume diffusive transport indeed predict a weak film thickness dependence simply due to small changes in NC volume fraction, but fail to rationalize the monolayer behavior. However, Monte Carlo simulations that account for quasi-ballistic heat carriers in the interstitial ligand matrix reproduce the experimental trends. Thus, our results suggest that ballistic heat carrier transport within the interstitial ligand could play a subtle role not previously revealed. We propose a picture in which thermal transport is dominated by the intrinsic interfaces within nanocrystalline composites, leading to strongly reduced thermal size dependence compared to typical thin films—with the exception of mono-to-few layers that moreover experience an enhancement due to non-diffusive heat transport between NCs. NC composites thus present an interesting material whose intrinsic bulk thermal properties extrapolate to the nanoscale and only deviate when single units are considered. These properties are important for the engineering of thermal management in NC-based applications.

2. Results and Discussion

2.1. Experimental Studies

2.1.1. Spatiotemporal measurement of nanocrystal supercrystals

The approach we take is to spatiotemporally probe lateral heat transport in several-micron domains of Au NC SCs with well-defined numbers of NC layers deposited on a glass coverslip (Figure 1). We assembled SCs of spherical Au NCs functionalized with polystyrene-thiol ligands (PSSH) by slow evaporation of colloidal solutions in toluene on a liquid subphase of diethylene glycol (see Methods).[40] The assemblies were then transferred to glass coverslips for optical microscopy and to transmission electron microscopy (TEM) grids for electron microscopy (see Methods). We studied three samples, featuring NC diameters of 26.4 ± 0.8 nm, 28.8 ± 0.8 nm, and 40.6 ± 0.6 nm, and PSSH ligand molecular weights of ~5 kg mol^{-1} ("PSSH5k") (26 and 41 nm NCs) and ~12 kg mol^{-1} ("PSSH12k") (29 nm NCs). The resulting Au NC SCs exhibit hexagonal packing with long-range order (Figure 1a,b, S1). The interparticle edge-to-edge distances were determined from TEM images of monolayers (Figure S1), giving 6.1 ± 0.9 nm, 6.8 ± 1.0 nm, and 4.4 ± 0.7 nm for the 26.4, 28.8, and 40.6 nm Au NC samples, respectively. Regions of varying number of SC layers, N_{layers}, ranging from 1 to about 10 can be readily identified by optical microscopy and were confirmed by correlative AFM (Figure S2, Table S1). Importantly, these regions persist with well-defined N_{layers} over the scale of several microns with few defects, making them large enough to probe by spatiotemporally-resolved thermoreflectance (Figure 1c).

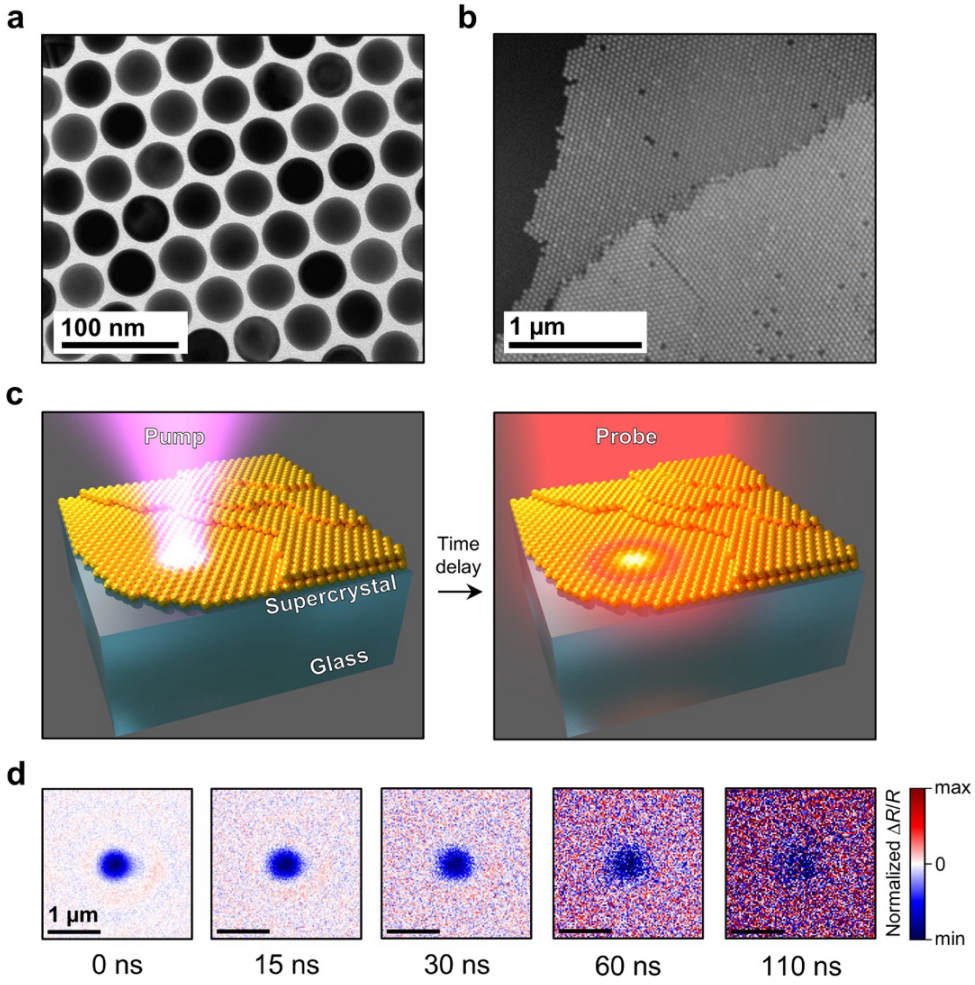

Figure 1. Spatiotemporal probe of thermal transport in mono- to few-layer nanocrystal supercrystals. (a) Transmission electron microscopy (TEM) image of a 40.6 nm Au–PSSH nanocrystal supercrystal monolayer. (b) Scanning electron microscopy (SEM) image of a region exhibiting monolayer and bilayer domains in the 40.6 nm nanocrystal supercrystal. (c) Schematic depiction of the spatiotemporally-resolved thermoreflectance technique in which a selected supercrystal domain is locally heated with a focused pump pulse and the subsequent lateral heat diffusion is imaged using a wide-field probe pulse. (d) Representative transient reflectance image time series in a monolayer supercrystal of Au–PSSH nanospheres. The linear time scale highlights the diffusive transport.

To locally resolve the lateral thermal transport and thermal relaxation to the substrate, we use spatiotemporally-resolved thermoreflectance (Figure 1c)—also known as stroboscopic optical scattering microscopy (stroboSCAT) in the configuration used here.[37,38,41] This approach has previously been applied to directly generate a Gaussian-shaped heat pulse and track its evolution in space and time in disordered nanosphere films and ordered nanorod SCs.[20,23,25,36] Here, we excite the Au NC SCs with 405 nm wavelength pump light pulses (≈100 ps) focused to a spot size of ≈340 nm (full-width at half-maximum). A repetition rate of 500 kHz ensures thermal relaxation between pulses. With an excitation fluence of ≈40 μJ cm^{-2} at 2σ of the Gaussian beam, we estimate an initial change in temperature of a few Kelvin (see Methods).[20] We image the resulting temperature profile in wide-field via temperature-induced changes of the reflectance, $\Delta R/R$, using 635 nm probe pulses (Figure 1c). The pump–probe time delay is typically controlled over 200 ns, during which time the transient temperature profile propagates by heat transport (Figure 1d). We fit the images to a two-dimensional Gaussian function of width σ to extract the mean-squared expansion curve, $\sigma^2(t) - \sigma^2(t_0)$. In the case of isotropic diffusive transport, the radial expansion of the Gaussian profile is related to

the diffusion coefficient by $\sigma^2(t) - \sigma^2(t_0) = 2Dt$. In this system we measure root-mean-squared expansions between ≈30–300 nm, meaning that regions about 1 μm in size are sufficient to probe thermal transport properties in an area-selective manner. We leverage this local probe to perform correlative spatiotemporally-resolved thermoreflectance and AFM to obtain the lateral thermal diffusivity for domains with known number of SC layers (Figure S2, Table S1). We note that, unlike typical thermoreflectance experiments,[4,17,19,34] no transducer layer is needed in the present case as the heat pulse can be generated directly within the metallic NC cores. This configuration avoids the need to account for the transducer–to–sample heat transfer timescale that could inhibit the separation of timescales needed to extract the SC thermal diffusivity below.

2.1.2. Identification of time scales

The spatiotemporal resolution of the measurement allows us to identify three dynamical processes corresponding to different steps in the cascade of heat transfer in an Au–PSSH NC SC monolayer in contact with glass (Figure 2a). In the first few nanoseconds, the mean-squared expansion exhibits a sublinear increase with time. By 10 ns the thermal transport reaches a diffusive regime (linear time dependence) with $D = 2.5 \times 10^{-3}$ cm^2 s^{-1}. Around 50 ns, the mean-squared expansion starts deviating from that regime, revealing an acceleration of heat transport at late times. The overall transient temperature increase relaxes with a 1/*e* time of about 10 ns and a slow tail limited by heat dissipation to the substrate (Figure 2b).

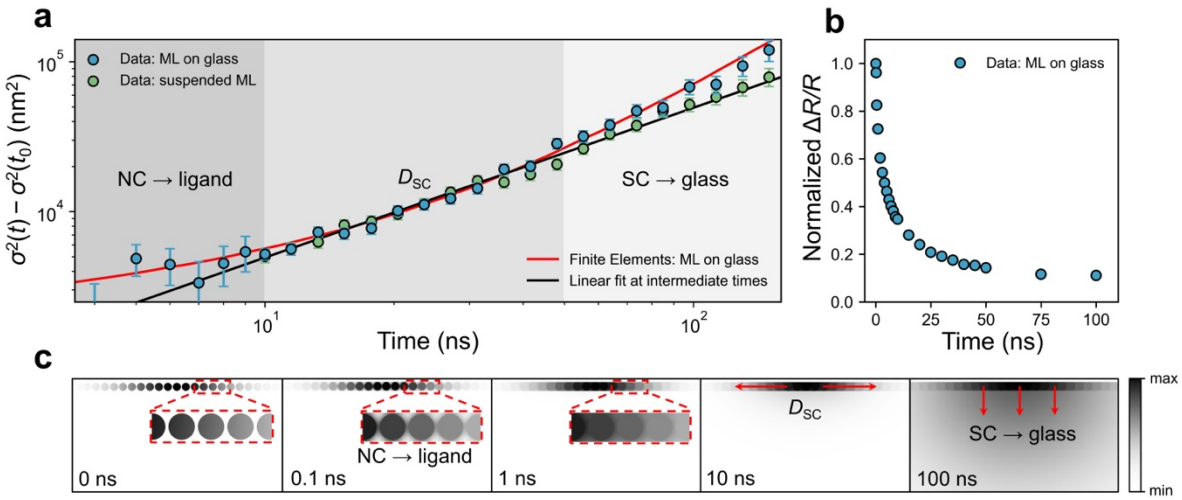

Figure 2. Experimental and simulated dynamic time scales and associated processes. (a) Comparison of experimental mean-squared expansion curves of thermal transport for a monolayer (ML) of 40.6 nm Au–PSSH5k nanocrystals in contact with a glass substrate (blue circles) and a suspended monolayer (green circles). The red curve corresponds to the mean-squared expansion of the simulated temperature profile in (c). The solid black line is a linear fit of the suspended monolayer data at intermediate times of 10–50 ns. The shaded gray regions distinguish different time regimes of nanocrystal-to-ligand interfacial thermal transfer (dark gray), diffusive thermal transport of the composite nanocrystal supercrystal (medium gray), and heat dissipation to the substrate (light gray). (b) Heat relaxation kinetics in a monolayer supercrystal in contact with a glass substrate. (c) Temperature profiles in a monolayer Au–PSSH nanocrystal supercrystal in contact with a glass substrate, computed by two-dimensional finite element simulations with associated time scales. Simulations were performed on a two-dimensional geometry with 40.6 nm Au circles, 4.4 nm gaps, and 4.4 nm top and bottom ligand layers, based on AFM results (Table S1, Figure S3, S4). Thermal parameters appear in the Methods.

We perform two-dimensional finite element simulations of thermal transport based on Fourier's law (see Methods). The simulations are solved as a function of time starting from a

Gaussian envelope of elevated NC temperatures in a geometry based on AFM measurements (Table S1, Figure S3, S4) to mimic the experiments. The simulations reproduce the experimental transport dynamics in Figure 2a with good agreement. We use these simulations as a guide for attributing a physical process to each of the three regimes (Figure 2c). The laser excitation of the pump exclusively heats the electrons within the NCs through the excitation of the Au d−s interband transitions, which rapidly thermalizes with the lattice via electron–phonon scattering on a picosecond time scale[20,42,43]—much faster than the instrument response function here. In the first nanoseconds, heat is transferred from the NC cores across the inorganic–organic interface to the neighboring ligands, resulting in slow transport. The simulations indicate a ~100 ps time constant for the interfacial transfer, though this is not directly accessed in the present experiments. Heat then travels across the inter-NC gaps via the interstitial ligand matrix. On a few nanoseconds time scale, heat reaches neighboring Au NCs, giving a monotonic temperature gradient between neighbors (Figure S5). This marks the delayed onset of the diffusive regime. The thermal diffusion coefficient during this time window can be considered as that of the effective medium of the composite NC–ligand SC (D_{SC}) spatially averaged over the NCs and ligand gaps. At later times, after about 50 ns in the case of the monolayer, heat transfers to the glass substrate, which has a higher diffusivity than the SC, resulting in an apparent increase in diffusivity.

We confirm that the intermediate time regime corresponds to the intrinsic transport properties of the SC by probing a suspended monolayer (Figure S6). In this case, the late-time acceleration due to the substrate is suppressed (Figure 2a). Importantly, the thermal diffusion coefficient measured in the suspended monolayer ($D = 2.5 \times 10^{-3}$ cm^2 s^{-1}) agrees with the value obtained at intermediate times for the monolayer in contact with glass (with overlapping mean-squared expansion curves). Similarly, finite element simulations yield agreeing SC thermal diffusivities when allowing or omitting transfer to the glass substrate if only the 10–50 ns time window is fit. Consistent with this picture, we find that for bilayer regions, the transition to faster transport from the substrate is delayed to about 100 ns in both experimental data and simulations, and for more layers the transfer to the substrate is progressively slowed beyond the time window we probe (Figure S7). Moving forward, we focus on the intermediate, diffusive time window under the interpretation that it yields the effective SC thermal diffusion coefficient D_{SC} without influence from the substrate.

2.1.3. Supercrystal thermal diffusivity as a function of thickness

The principal focus of this work is the relationship between thermal transport and the number of NC SC layers. We perform correlative spatiotemporally-resolved thermoreflectance and AFM (Figure 3a,b, Table S1) to extract the thermal diffusivity in domains with 1 to 8 SC layers, corresponding to about 30–320 nm in thickness (Figure 3c). We report two key observations. We find that the thermal diffusivity D_{SC}: (1) is constant within error for the few-to-multilayer range, and; (2) it exhibits an enhancement when the thickness is reduced down to a monolayer (Figure 3c). We measure the monolayer thermal diffusivity to be 30% to 60% higher than the multilayer diffusivity for the samples studied here.

Such behavior is in stark contrast to typical thin film materials that experience decreasing thermal diffusivity as the film is made thinner. We emphasize that this trend is robust for three different Au NC SCs with varying diameters and for different PSSH ligand lengths. Measurements were averaged over multiple locations of the SCs, the measured diffusivity does not depend on pump fluence or exposure time, and no sign of film degradation was observed. Moreover, the thermal diffusivity of the monolayer is not altered by contact with the glass substrate (Figure 2). Next, we pursue several models to uncover the mechanistic origin of this inverted thermal size effect behavior and constant multilayer thermal diffusivity.

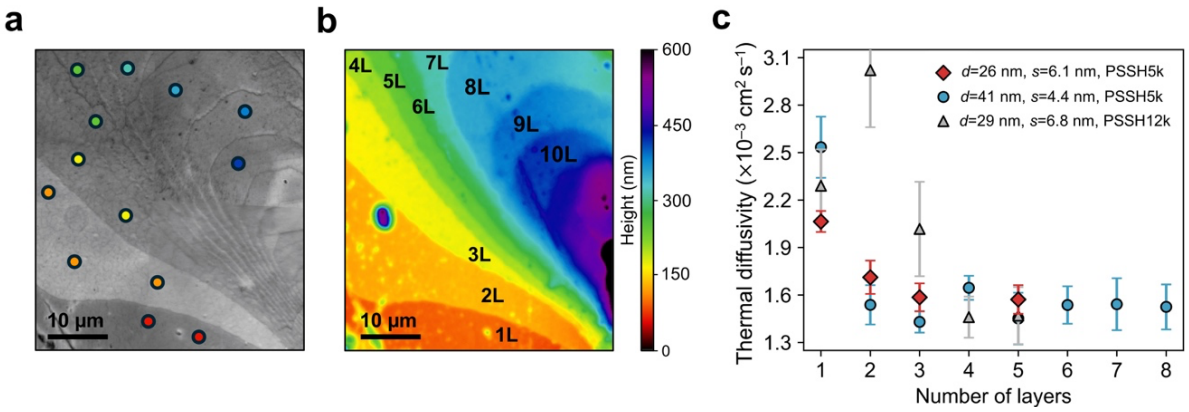

Figure 3. Supercrystal thermal diffusivity dependence on number of supercrystal layers. (a) Optical microscopy image of a typical mono- to few-layer nanocrystal supercrystal. Circles show example locations where pump–probe measurements were performed. (b) AFM image of the same area shown in (a) with the number of supercrystal layers labeled. (c) Au nanocrystal supercrystal thermal diffusivity as a function of the number of nanocrystal layers for three different samples with different nanocrystal diameters (d) and inter-nanocrystal gaps (s). Each data point is obtained by averaging a series of five to ten measurements taken in different locations, and the error bars correspond to the standard deviations of such series.

2.2. Modeling of thickness dependence

2.2.1. Breakdown of diffusive thermal transport

We first rule out variations in typical thermal parameters such as volume fraction, density and heat capacity as a function of NC layers as origins of the anomalous thickness dependence. In a purely diffusive picture (heat flow described by Fourier's law), the Hasselman and Johnson formulation of the effective medium approximation (EMA) can be used to express the effective thermal conductivity of a composite medium as a function of each component's volume fraction, thermal properties, and the interfacial thermal conductances.[44] It has been shown that this model reasonably reproduces the thermal conductivities of a large range of bulk, three-dimensional NC solids.[17–19] Here, in the case of hexagonal packing of a finite number of layers, the Au volume fraction increases with the number of layers because the spheres of each new layer lie in the interstices left by the underlying NCs (Figure 4a, S3). We calculate the resulting thermal diffusivity versus the number of SC layers (see Methods), focusing on the diffusivity relative to a 10-layer SC, D/D_{10L}, for better comparison between all models. Instead of the experimentally observed trend, the EMA predicts an increasing thermal diffusivity (and thermal conductivity) as more layers are added to the SC (Figure 4b). This is because the relative proportion of the highly conductive material increases and outweighs the slight decrease in heat capacity. To ensure that this shortcoming is not due to an artifact of edge effects or time-dependent processes not accounted for in the EMA, we perform two-dimensional finite element simulations (see Methods) and extract the thermal diffusivity in the diffusive regime >10 ns as a function of N_{layers} (geometry appears in Figure 4a and Figure S4). The simulations overlap the EMA result within numerical precision, showing increasing D_{SC} with increasing N_{layers}. The dimensionality makes only a minor difference, with two- and three-dimensional EMA calculations nearly overlapping (Figure 4b), suggesting that two-dimensional simulations should have been sufficient for semiquantitative trends. The inability of the EMA model and finite element simulations to describe the trend of the experimental data indicates a need to explore dynamics beyond the diffusive regime.

We note that an enhanced monolayer diffusivity can be compatible with diffusive thermal transport in the limit of very low interfacial thermal conductance between the NCs and the ligands (Figure S8). In that limit, the NCs behave almost like non-conductive objects. D_{SC} thus decreases as more SC layers are added because the proportion of highly resistive interfaces increases. However, the interfacial conductances required to reach this regime would need to

be more than one order of magnitude below the estimated Au–PSSH interfacial conductance in our samples. Such low interfacial thermal conductances would in turn make the EMA model predict a D_{SC} well below what is measured here. Thus, we believe this model to be inadequate.

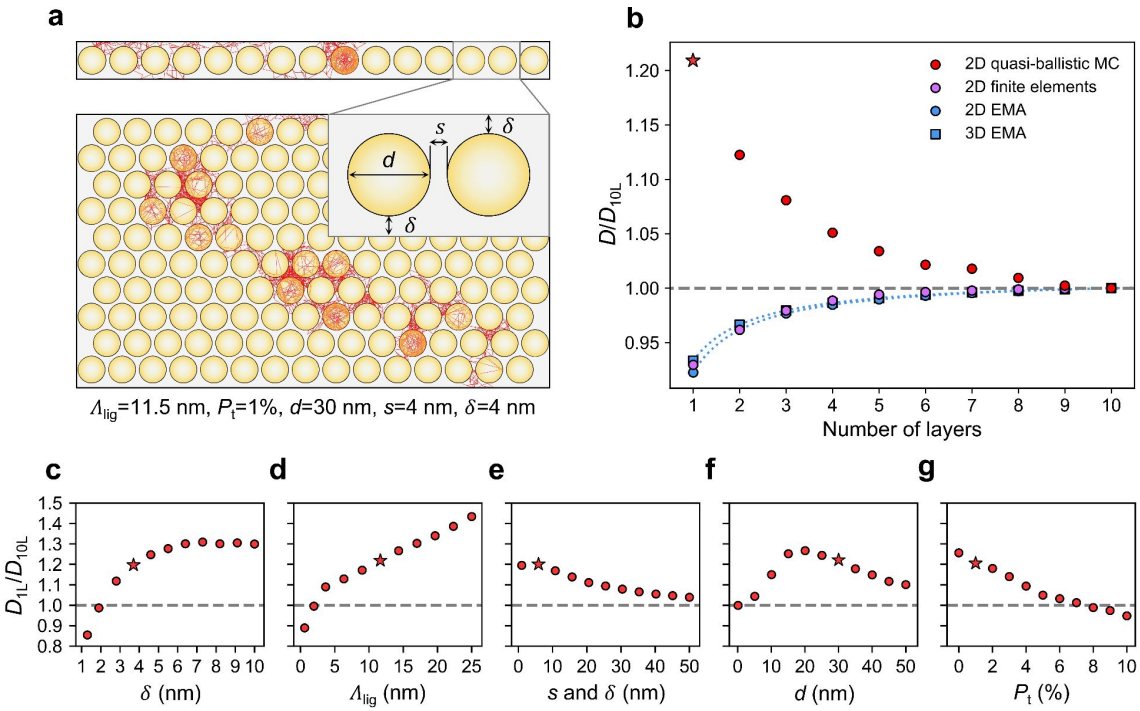

Figure 4. Simulations of thermal transport in mono- and multi-layer nanocrystal supercrystals. (a) Representation of the monolayer and multilayer simulation geometries with example phonon trajectories in red. The inset depicts the definitions of the geometric parameters for the nanocrystal (yellow regions) and ligand (gray regions). A larger, zoomed-in version of this figure appears as Figure S9. (b) Comparison of diffusivities with respect to the multilayer diffusivity (D/D_{10L}) in the EMA model, finite element simulations, and quasi-ballistic Monte Carlo simulations. (c-g) Ratio of monolayer and multilayer thermal diffusivities as a function of (c) top and bottom ligand layer thickness δ, (d) bulk ligand mean free path Λ_{lig}, (e) inter-NC spacing s with $\delta = s$, (f) NC diameter d, and (g) NC–ligand interfacial transmission probability P_t. The red star in each panel indicates the ratio D_{1L}/D_{10L} obtained for the base set of parameters used in (a). The geometric parameters used for all EMA calculations and simulations in this figure were: d = 30 nm, s = 4 nm, δ = 4 nm unless otherwise noted. Material thermal parameters appear in the Methods.

2.2.2. Beyond diffusion: ballistic effects

To rationalize the enhancement in thermal transport at the monolayer, we explore the role of ballistic heat carrier transport in ultrathin NC assemblies. We turn to Monte Carlo simulations of quasi-ballistic transport (see Methods). Thermal transport is modeled by straight movements of effective heat carriers at constant velocity that randomly scatter after encountering interfaces or traveling a distance equal to their mean free path, Λ (Figure 4a). This particle-like picture is motivated by previous reports that propagative localized oscillators rather than coherent phonon modes dominate heat transport in amorphous materials.[45] The particle picture of heat transport has previously been invoked for NC solids as well.[26] We place ourselves in the framework of "gray" Boltzmann transport where the mean free paths and group velocities of the energy carriers are frequency-averaged. This effective phonon approximation is motivated by the relatively narrow overlap between the Au and ligand vibrational density of states, allowing only similar energy (few-THz) phonons to cross the NC-ligand interface and dominate heat transport.[17,18,27,28]

Although the mean free path of heat carriers in the Au NC cores (Λ_{Au} = 38 nm) is similar to their size (d = 26–41 nm here), scattering within the NC cores is fixed as a function of N_{layers}. Thus, one might expect changes in the ligand geometry to dominate the thickness dependence. In the specific case of amorphous polystyrene, molecular dynamics simulations[46] suggest that, because vibrations propagate along the long carbon backbone of the polymer with minimal scattering,[47] the effective phonon mean free path is around Λ_{lig} = 11.5 nm. The NC-ligand interfacial thermal resistance is modeled in terms of a transmission probability P_t for crossing the interface each time a carrier reaches the NC–ligand interface (see Methods). We use a default value of P_t = 1%, estimated from literature values (see Methods).

The geometry of the SC plays a crucial role when there is ballistic transport. The geometry used in the simulations consists of a two-dimensional lattice of hexagonally packed Au circles embedded in a ligand matrix. Importantly, AFM measurements (Table S1) indicate that the SCs have ligand layers on the top (between the top of the top-most NC cores and the air) and bottom (between the bottom of the bottom-most NC cores and the substrate), each with thickness δ about equal to the inter-NC spacing (Figure 4a, S3, Table S1). Moreover, we assume that the long polymer ligands reorganize to minimize the surface area of the interface with other media and maximize overlap with neighboring NCs,[48–50] ultimately forming a flat interface with the air and substrate. As default parameters we use a NC diameter (d) of 30 nm, an inter-NC spacing (s) of 4 nm, and top and bottom ligand layer thicknesses (δ) of 4 nm as representative of the samples measured.

In order to obtain the lateral thermal diffusivity, we compute the horizontal mean-squared displacement as a function of time for a population of more than 10^5 particle trajectories subject to the sample geometry. Figures 4b and 4d show that, going from a diffusive to a ballistic regime effectively reverses the trend from an increasing to a decreasing thermal diffusivity when increasing the number of NC layers, thus aligning it with experimental observations. The simulation results agree with the magnitude of the enhancement of the monolayer diffusivity compared to that of the multilayer with only a slight underestimation. We note that we performed two-dimensional simulations with plausible parameters from the literature rather than fine-tuning them to fit the data precisely.

Particle trajectories (Figure 4a, S9) help to provide an intuitive picture for the thermal transport enhancement when approaching monolayer NC SCs. The horizontal channels in the top and bottom ligand layers allow phonons to efficiently move laterally with few scattering interfaces (Figure S10). In the monolayer, these channels make up a larger fraction of the vertical extent of the system. As more NC layers are added, the SC geometry imposes new tortuous paths that become more dominant and the overall lateral transport is increasingly hindered, leading to faster thermal transport in the monolayer with respect to the multilayer.

We tune simulation parameters one at a time to learn their impact on D_{1L}/D_{10L} (Figure 4c-g), using reference parameters of Λ_{lig} = 11.5 nm, P_t = 1%, d = 30 nm, and $\delta = s$ = 4 nm. The magnitude of the film thickness effect increases and progressively saturates with increasing top and bottom ligand layer thickness by allowing more trajectories with lateral path lengths larger than the mean free path (Figure 4c). While maximized for long phonon mean free paths in the ligand matrix, the enhancement effect vanishes when the mean free path gets smaller than the inter-NC spacing (Figure 4d,e). In that case, we enter the diffusive limit across all relevant length scales and the governing parameters become the relative proportions of ligand and Au, as predicted by EMA. For very small and very large NCs, the system tends either to bulk PSSH or Au, respectively, with no monolayer enhancement (Figure 4f). Interestingly, for high transmission probabilities (large interfacial thermal conductance), available routes through the NCs weaken the confinement caused by the inter-NC spacing and the monolayer enhancement is reduced (though the absolute diffusivity increases) as the proportion of Au simply dominates (Figure 4g).

2.3. Summary of mechanism

We attribute the physical origin of the thickness dependence of the thermal diffusivity of NC SCs to heat transport being dominated by phonon scattering at the NC–ligand interfaces. The thermal size effect in most materials typically originates from phonon scattering at the boundaries of the material or grain boundaries within the material, leading to a decrease in thermal conductivity with decreasing size when the material dimensions are comparable to and smaller than the phonon mean free path. In contrast, the NC SC can be thought of as an effective bulk thermal medium with controllable, fixed nanograin size,[26] diminishing any effects from the finite thickness of the overall material, nearly down to the monolayer. In this picture, the NC size and arrangement set the mean free path independent of overall thickness. In other words, concerning its thermal transport properties, this system effectively reaches bulk starting at even a few layers. Empirically, our observation of film thickness-independent thermal transport above a few SC layers points to a very small phonon mean free path on the order of single SC layers or shorter despite the long-range SC ordering. Our quasi-ballistic heat carrier simulations elaborate on this point, suggesting average free path lengths shorter than the NC size within the interstitial ligand and about equal to the NC diameter within the NCs. Still, the mean free path is long enough for non-diffusive transport to take advantage of straight paths within the SC geometry. In this picture, the inverted thickness dependence of thermal transport occurs because of heat carriers being ballistically channeled through straight paths in the top and bottom ligand layers.

We expect such behaviour to be general in assemblies of NCs with ligands in which the phonon mean free path is longer than the NC spacing. These notions are consistent with previous findings that heat transport is dominated by elastic vibrational scattering at the NC–ligand interface such that the overlap in the vibrational density of states of the two materials limits the phonon modes responsible for heat conduction in the composite medium to those in the few THz range (few to ten meV).[17,26–28] We also consider that ordered NC SCs should also support collective, low-energy SC phonons with long mean free paths.[9,22,51] However, recent studies demonstrated that such modes do not significantly contribute to heat conduction in NC SCs.[22,28] Taken together, the above points mean that beyond a few layers, Fourier's law and interfacial thermal transfer capture the essential trends of NC SCs, but at the scale of NC units ballistic transport effects should be considered.

It is interesting to consider a hydrodynamic description of thermal transport as an alternative physical picture.[52,53] The gray Boltzmann transport model implemented above is compatible with the emergence of heat viscosity effects at moderate ratios of heat carrier mean free path to system size.[54] In this picture, curved paths between NCs would lead to a viscous reduction of the apparent conductivity for thick SCs compared to a monolayer. Such a model warrants detailed investigation that we do not elaborate on here.

2.4. Implications for nanocrystal applications

The absent thickness dependence for multi-layer NC assemblies—and moreover inverted behavior for mono-to-few layers—stands in contrast to typical materials over a comparable 30–320 nm thickness range. In materials ranging from metals and semiconductors to oxides and amorphous polymers, thermal conductivities decrease by ≈30–70% over the same thickness range, and even more compared to their bulk values.[29–31,46,55–57] The case of NC SCs also is very different from layered two-dimensional materials[31] as well as quantum well superlattices that might be considered more comparable.[58,59] For example, Sood et al. found a significant reduction to ≈60% in thermal conductivity with decreasing thickness in layered MoS_2 for the same thickness range due to quasi-ballistic phonon transport with mean free paths extending hundreds of layers.[31] Suspended monolayer graphene is an exception for which an inverted layer dependence has also been reported, though by a different mechanism.[60] Broadly speaking, we expect an attenuated film thickness dependence to be common for NC assemblies

for a wide range of core and ligand materials, NC core size, and ligand lengths because in all cases the thermal conductivities of NC arrays are dominated by NC–ligand scattering.[61] Even in the case of negligible ballistic transport that may occur for other NC sizes or ligands, the ≈10% decrease in thermal diffusivity due to volume fraction predicted by simulations and EMA would still constitute a notably weak thermal size effect.

Our findings have important implications for the engineering of colloidal NC-based applications in general, and we also identify NC films as a material with particular nanoscale thermal properties. For optoelectronics, nanoelectronics, plasmonics, and catalytic systems featuring thin NC films, efficient thermal dissipation is typically targeted. Meanwhile, in the context of thermoelectrics, independent control of thermal and electronic transport properties is crucial to function. The observation of an effective lack of film thickness dependence means that, unlike common materials, one can arbitrarily reduce the dimensions of the NC film down to few layers without changing its thermal properties. This suggests that, again unlike most materials, heat dissipation is not slowed by making a film thinner. Practically speaking, convenient measurements of thermal conductivity can be performed on thick multilayer NC films and be expected to hold relatively constant even down to very thin films of only a few SC layers. For instance, the thermal dissipation timescale for thin NC films can be simply predicted with reasonable accuracy using the bulk conductivity and the ligand–substrate interfacial resistance. Approaching the monolayer is an exception when using ligands with large mean free path, instead giving an enhancement compared to the bulk. This boost to heat dissipation at the monolayer could be highly beneficial for applications of thin SCs, such as LED emitting layers, field-effect transistors and catalysis. While the number of NC SC layers does not strongly change the intrinsic properties, we recall that the thermal conductivity itself can be moderately controlled through the NC volume fraction (i.e., NC core size, ligand length, packing structure), NC ordering, and temperature, while changing the NC core material results in relatively minor changes.[2,3,9,17–19,22,23,26] Exchanging to short ligands—as is often done to increase electronic coupling—may decrease the phonon mean free path in the ligand and in turn the monolayer enhancement (Figure 4d). According to our simulations, common quantum dot assemblies that feature ≈5 nm NCs and short 0.5 nm ligands (assuming a mean free path equal to the ligand length) exhibit a reduced thickness dependence with $D_{1L}/D_{10L} \approx 1.06$. The above points are highly relevant to NC thermoelectrics in addition to optoelectronics and nanoelectronics.[2,4,7,26]

Our work indicates another interesting property of NC assemblies, which is that materials in contact with the boundary of the NC film do not significantly perturb its internal thermal transport. In common thin film materials, this interaction with the boundary is precisely the cause of the thermal size effect. In contrast, in the NC SC the NC size and inter-NC spacing sets the upper bound on the heat carrier mean free path. However, the substrate will still affect the thermal dissipation timescale though the ligand–substrate interfacial thermal conductivity. Film thickness and substrate may be the most readily controllable parameters to substantially engineer heat dissipation in NC solids.

3. Conclusion

In this work, we have accessed the lateral thermal diffusivity of Au NC SCs down to the monolayer. This was achieved using correlative spatiotemporally-resolved thermoreflectance and AFM, which is a powerful approach for unveiling structure–thermal property relationships. By leveraging the time resolution of our technique and studying heat transport after it has overcome the ligand barrier but before it has been transferred to the substrate, we are able to extract the intrinsic thermal properties of monolayer and few-layer SCs. We confirmed the hypothesis that NC assemblies exhibit a weak thickness dependence compared to traditional materials with a thermal diffusivity that is nearly independent of film thickness down to a few SC layers. This suggests that the mean free path of phonon modes responsible for heat

conduction is primarily limited by the intrinsic interfaces of the nanocrystalline composite material. Going even thinner, mono- to few-layer NC SCs exhibit an enhanced thermal diffusivity of 30–60% compared to the bulk that can be rationalized with a quasi-ballistic heat carrier model. Our work suggests that the ballistic nature of phonons can play a substantial role in the thermal conductivity of NC solids. While Au-based nanocrystals with long-chain organic ligands were used as a model system in this study, a minimal thickness dependence is expected to occur in other materials such as smaller quantum dots and with short ligands. The fact that the thermal properties of such materials do not change when reduced to single-layer nanofilms is unusual and is important knowledge for the engineering of devices made from nanocrystals. This phenomenon presents potential for the bottom-up design of thermal management. As Moore's law continues to be pushed, the importance of thermal management at the nanoscale becomes increasingly important, and NC-based systems present unconventional properties that may be exploited.

4. Methods

Materials: Hydrogen tetrachloroaurate trihydrate ($HAuCl_4 \bullet 3H_2O$, ≥99.9%), sodium borohydride ($NaBH_4$, >98%), cetyltrimethylammonium bromide and chloride (CTAB and CTAC, ≥98%)and L-ascorbic acid (99%) (all Sigma Aldrich, USA), toluene (≥99.5%), tetrahydrofuran (≥99.5%), and ethanol (denat., >96%, VWR), diethylene glycol (DEG, reagent grade, Merck, Germany) and thiolated polystyrenes (PSSH, $M_n = 5300$ g mol^{-1}, $M_w = 5800$ g mol^{-1}, PSSH12k: $M_n = 11{,}500$ g mol^{-1}, $M_w = 12{,}400$ g mol^{-1}, Polymer Source, Canada) were used as received. Ultrapure water (resistivity: 18.2 MΩ•cm) was used for all preparations.

Synthesis, functionalization and assembly of Au nanospheres: The Au nanospheres where synthesized and assembled following established protocols.[32,62] In brief, the synthesis is a seeded-growth protocol with cetyltrimethylammonium chloride as a capping ligand, which is then exchanged with thiol-terminated polystyrene-ligands (here with average molecular weights of ~5000 g mol^{-1} ("PSSH5k") and ~12000 g mol^{-1} ("PSSH12k")) by phase-transfer into tetrahydrofuran and finally into toluene. The purified dispersions of polystyrene-capped Au nanospheres in toluene are then pipetted onto a liquid subphase (DEG) in a teflon well. Slow evaporation of the toluene then leads to well-ordered self-assembly of the Au nanospheres into thin-film supercrystals with layer numbers ranging from mono- to multilayers. Because the thin-film supercrystals form freely-floating on an immiscible liquid subphase, they can be easily transferred to the required substrates. TEM grids are held by a tweezer and carefully immersed into the subphase below the sample, which is then skimmed off. To deposit the films onto glass substrates, these can be immersed into the liquid subphase. Then the liquid subphase (DEG) is carefully removed with a pipette so that the sample deposits onto the glass substrate. This also works when the substrate is tilted. If the glass substrate is too large to be immersed into the teflon well containing the liquid subphase, the following method can be used: additional DEG is carefully added with a pipette into the liquid subphase, thereby lifting its meniscus. Once the meniscus reaches the level of the well opening, its convex shape (due to surface tension) allows careful insertion of the substrate below the floating thin-film supercrystal sample. Then the remaining DEG on the substrate is removed with a pipette so that the sample deposits onto it. For all these methods, after depositing the sample, DEG is removed without damaging the sample by careful pipetting or dabbing with a small piece of tissue around the sample area. TEM grids can also be dabbed carefully onto a filter paper with their bottom side so that DEG is soaked from below. Remaining DEG is further removed under reduced pressure/vacuum using an oil pump. A more detailed description of the synthesis and characterization of the materials can be found in a previous report.[32]

Transmission electron microscopy (TEM): TEM samples of self-assembled Au nanosphere films were prepared by carefully skimming off the liquid subphase with a carbon-coated copper grid (400 mesh), held by a tweezer, then dried in vacuum for at least 1 h. These samples were measured with a JEOL 1011 at 100 keV and the measurements analyzed with Image-J.

Scanning electron microscopy (SEM): The Au nanosphere supercrystals were imaged using a Zeiss Sigma SEM operated with a 10 kV acceleration voltage.

Atomic force microscopy (AFM): AFM of the same Au nanosphere supercrystal domains measured by spatiotemporally-resolved thermoreflectance was performed using an NX20 AFM (Park Systems) equipped with a PPP-NCHR 10M non-contact cantilever (Park Systems). Images were collected in non-contact mode. Images were flattened and corrected using Gwyddion.[60] The film thickness was determined by comparing relative heights of the layers relative to the glass substrate.

Optical microscopy: Optical microscopy images were collected on the spatiotemporally-resolved thermoreflectance setup using a white-light light emitting diode (LED) (MNWHL4, ThorLabs) and an adjustable collimating lens (SM1U25-A, ThorLabs) with a LED driver (T-Cube LEDD1B, ThorLabs).

Spatiotemporally-resolved thermoreflectance measurements: The experimental setup for measurements of spatiotemporally-resolved thermal diffusion was previously described in detail[25] and was based on an instrument developed by Delor et al.[37] Briefly, the home-built microscope used an inverted microscope configuration with a NA = 1.4 oil-immersion objective. Laser diodes with center wavelengths of 405 nm (LDH-D-C-405, PicoQuant) and 635 nm (LDH-D-C-640, PicoQuant) and <100 ps pulse durations were used for the pump and probe beams, respectively, and were operated by PicoQuant drivers to electronically control the pump–probe time delay. We used a laser repetition rate of 500 kHz, with the pump modulated at 660 Hz. Both the pump and probe were spatially filtered through pinholes, the probe beam passed through a wide-field lens, the two beams are overlapped using a dichroic mirror and reflected into the objective by a 50/50 beamsplitter. This leads to an overlapped near-diffraction-limited pump and wide-field probe illumination. Probe light reflected from the sample was collected through the same objective, isolated with a band-pass filter and focused onto a CMOS camera, triggered at 660 Hz by the laser driver. The pixel calibration was done using a 1951 USAF Pattern resolution target (R3L1S4PR, Thorlabs), giving 28 nm/pixel. Pump–probe images are generated by taking the difference between pump-on and pump-off raw pixel intensities, normalized to the raw pump-off intensities, yielding $\Delta R/R$ contrast images as a function of time delay. Data acquisition was implemented in LabVIEW 2022 64-bit. Data analysis and plotting were performed using Python. All measurements were performed at an ambient temperature of 293 K.

The pump fluence was calculated by measuring the power arriving at the sample position—using a microscope slide format power sensor (S171C, Thorlabs) and power meter (PM100D, Thorlabs)—and measuring the pump spot size (340 nm at FWHM) by imaging its reflection. The Au NC films were excited with a 2σ-integrated fluence of ≈40 μJ/cm^2, corresponding to an approximate temperature rise of a few Kelvin after lattice equilibration (see estimation of absorption length below).[14] In principle it is possible that the photoexcitation can alter the sample over the course of a measurement. However, we verified that the measured diffusivities did not depend on pump fluence over the range of 30–100 μJ/cm^2, and we ensured that no sign of film damage was observed at the pump fluence used.

To obtain the relaxation and mean-squared expansion curves, each $\Delta R/R$ image of a given spatiotemporally-resolved thermoreflectance time series is fitted to a normalized two-dimensional Gaussian profile function with a common center and floating amplitudes and widths. The optimal center is determined using the Nelder-Mead algorithm to minimize the total sum of squared residuals between the entire series of pump–probe images and 2D gaussian functions. The width of the Gaussian σ versus time t is used to obtain the mean squared expansion, $\sigma^2(t) - \sigma^2(t_0)$.

Estimation of nanocrystal supercrystal temperature jump: To estimate the photoinduced temperature jump in the Au NC film, we assume that all the energy of the absorbed photons is converted to heat because they are metallic. Assuming that the electron heat capacity is negligible compared to those of the NC lattice and film, the pump-induced film temperature jump is $\Delta T = U/\rho C_p$, where U is the absorbed energy, ρ is the film mass density, and C_p is the film specific heat capacity. We use the average mass density—$\rho = \varphi_{NC}\rho_{NC} + (1 - \varphi_{NC})\rho_L$, where φ_{NC} is the volume fraction of the NC core and ρ_{NC} and ρ_L are the densities of the NC core and ligand, respectively—and the mass-weighted specific heat capacity—$C_p = m_{NC}C_{NC} + (1 - m_{NC})C_L$, where m_{NC} and $1 - m_{NC}$ are the mass fractions of the NC core and the ligand, respectively, and C_{NC} and C_L are the NC core and ligand specific heat capacities, respectively.

The volumetric heat capacity increases marginally 1.7–1.8 × 10^6 J m^{-3} K^{-1} going from monolayer to eight layers. The absorbed energy is given by $U = J_0(1 - 10^{-A})/L$, where J_0 is the pump fluence, A is the film absorbance, and L is the film thickness. J_0 was simply determined from the pump power and spot size to be ≈40 μJ/cm^2 at 2σ. We find A by measuring the absorption of a focused laser beam through a sample of known L as determined by AFM. With the sample mounted on a glass coverslip on the spatiotemporally-resolved thermoreflectance microscope, the focused 405 nm beam used for the pump source was positioned within an optically smooth region of a SC domain. The power passing through the SC relative to the power passing through a blank region of coverslip was measured using a S171C silicon photodiode power sensor and PM100D power meter (Thorlabs). Taking the 41 nm Au NC SC as a representative sample, the absorbance was found to be 0.50 to 2.0 when going from monolayer to eight SC layers. Taken together, we calculate a temperature jump in the range of 0.5–3 K.

Finite element simulations: COMSOL Multiphysics® 6.0 (COMSOL Inc., Los Angeles, CA) finite element software was used to simulate heat transport in the Au NC films. The simulations were conducted using the built-in Heat Transfer in Solids module. To render the simulations computationally feasible, we reduce the geometry to two dimensions, including the in-plane (parallel to the substrate) and out-of-plane (perpendicular to the substrate) thermal transport. Simulation geometries were constructed using a simplified rectangular region to act as the interstitial ligand which was then embedded with a vertically stacked hexagonal NC lattice consisting of 1 to 10 layers. Based on the TEM images of the NC film, we modeled Au–PSSH NCs as 41 nm diameter Au circles with 4.4 nm inter-NC gaps (Figure 2) or 30 nm NCs with 4 nm gaps (Figure 4). The bottom of the composite film was in contact with glass while the top was in contact with air, both separated from the nearest NC edges by 5 nm—the observed inter-NC gap size. Au NC cores were given the properties of bulk Au: a density of 19,300 kg m^{-3}, thermal conductivity of 310 W m^{-1} K^{-1}, and heat capacity of 129 J kg^{-1} K^{-1}. For the interstitial PSSH, we assumed a density of 1000 kg m^{-3},[6] thermal conductivity of 0.15 W m^{-1} K^{-1}, and heat capacity of 1250 J kg^{-1} K^{-1} based on polystyrene thin films as a proxy.[63] The Au–PSSH interface is treated as an equivalent thin resistive layer assuming a layer conductance of 50 MW m^{-2} K^{-1} (see discussion below for estimation). The PSSH–glass interface has a layer conductance of 4 MW m^{-2} K^{-1} based on reports of polystyrene film–sapphire interfaces as a proxy.[64] Thermal transfer to the air above the film was neglected. The lateral size of the film and width of the glass substrate were large enough to avoid edge effects in the thermal transport. 300 K was used as the ambient reference temperature, and simulations were initialized using a Gaussian profile (sigma = 180 nm) of elevated temperature with a peak of 310 K (ΔT_{max} = 10 K), reflecting the experimental conditions. The mesh was constructed using a "fine" element size. The finite element simulation solves the heat equation (Fourier's law) using a quadratic Lagrange discretization to calculate the time dependence of the temperature profile with a relative tolerance of 0.0001. The simulated temperature profiles as a function of time were treated analogously to the stoboSCAT data, fitting to a Gaussian function over time and calculating $\sigma^2(t) - \sigma^2(0)$ to produce mean-squared expansion curves and thereby extract the diffusivity by fitting to $2Dt$ in the diffusive time regime. The contact with the substrate was removed when determining the simulation values for D_{SC} to avoid mixing with the effects from the substrate and fitting was performed for the diffusive regime >10 ns.

Estimation of interfacial thermal conductance of Au–PSSH. The interfacial thermal conductance between the Au NCs and the PSSH ligands was estimated by assuming that the thermal transfer per ligand is governed by the Au–thiolate binding and ligand grafting density, σ. Thus, we take the known interfacial thermal conductance (220 MW m^{-2} K^{-1})[18] and ligand grafting density (4.8 ligands/nm^2)[18] for Au-dodecanethiol self-assembled monolayers (SAM) and adjust for the reduced ligand coverage of the bulk polymer ligands—cited to be about 1

ligand nm^{-2}.[6,32,49] This assumption is based on previous work that showed that the interfacial thermal conductance $h_{\text{NC–ligand}}$ is proportional to ligand grafting density, which in turn is radius (r) or surface curvature dependent such that $h_{\text{NC–ligand}}(r)/h_{\text{NC–ligand}}(\text{SAM}) = \sigma(r)/\sigma(\text{SAM})$.[18] Plugging in the values above gives $h_{\text{NC–ligand}} \approx 50$ MW m^{-2} K^{-1}, which is the value used in our finite element simulations.

Effective medium approximation (EMA): We find that EMA calculations of thermal diffusivity do not correctly predict the Au–polystyrene-thiol NC SC thickness dependence approaching the monolayer, but do predict an overall weak thickness dependence. Here we describe our calculations. Derived in the diffusive regime from Fourier's law, the Hasselman Johnson Maxwell Euken formulation of the EMA has been established to work well in the case of multilayer NC solids.[17,18,44] The effective thermal conductivity of the composite medium, k_{eff}, is given by the equation:

$$k_{\text{eff}} = k_{\text{lig}} \frac{2\left(\frac{k_{\text{NC}}}{k_{\text{lig}}} - \frac{k_{\text{NC}}}{rh_{\text{c}}} - 1\right)\varphi_{\text{NC}} + \frac{k_{\text{NC}}}{k_{\text{lig}}} + \frac{2k_{\text{NC}}}{rh_{\text{c}}} + 2}{\left(1 - \frac{k_{\text{NC}}}{k_{\text{lig}}} + \frac{k_{\text{NC}}}{rh_{\text{c}}}\right)\varphi_{\text{NC}} + \frac{k_{\text{NC}}}{k_{\text{lig}}} + \frac{2k_{\text{NC}}}{rh_{\text{c}}} + 2}$$

where k_{lig} is the ligand thermal conductivity, k_{NC} the NC core thermal conductivity, r the NC core radius, h_{c} the NC–ligand interfacial conductance, and φ_{NC} the NC core volume fraction. Then, the effective diffusivity of the composite medium can be calculated as $D_{\text{eff}} = k_{\text{eff}}/\rho C_{\text{p}}$. Here, ρ is the composite mass density, while Malen and coworkers showed that, specifically, the mass-weighted average specific heat capacity C_{p}, is appropriate for NC arrays.[17]

Within the framework of the EMA, k_{eff} changes due to changes in the volume fraction, assuming that the inter-NC spacing, ligand density, and ligand grafting density remain constant as a function of NC SC thickness. D_{eff}, in turn, comprises changes in density and heat capacity as well. We assume that the long polymer ligands reorganize in a way that minimizes the surface area of the interface with other media. This means that the ligand layer forms a flat interface with the substrate and air for simplicity. We note that using a circular/spherical shell does not change the qualitative trend.

As we compare EMA to the results of finite element and quasi-ballistic Monte Carlo simulations, which are two-dimensional, we first use area fractions, α_{NC}, as a substitute for volume fractions. We find the area fraction for hexagonally-packed two-dimensional lattice of circles of N_{layers} rows between two flat interfaces is:

$$\alpha_{\text{NC}} = \frac{1}{2}\left(\frac{d}{d+s}\right)^2 \frac{\pi N_{\text{layers}}}{2 + \sqrt{3}(N_{\text{layers}} - 1)}$$

where N_{layers} is the number of layers, d is the NC diameter and s the inter-NC spacing. In the bulk limit ($N_{\text{layers}} \to \infty$), we recover the area fraction of circles in a hexagonal unit cell, $\alpha_{\text{NC, bulk}} = \pi d^2/[2\sqrt{3}(d+s)^2]$. We take eight or ten layers to be a good approximation of the bulk as evidenced by the plateau in the diffusivity versus thickness curve seen in Figure 4b.

To account for the three-dimensional nature of the hexagonally-packed spherical NCs, we find the NC volume fraction for spheres. We assume hexagonal close packing[32] and that the ligands form flat interfaces with the air and glass, giving:

$$\varphi_{\text{NC}} = \frac{1}{3}\left(\frac{d}{d+s}\right)^3 \frac{\pi N_{\text{layers}}}{\sqrt{3} + \sqrt{2}(N_{\text{layers}} - 1)}$$

In the bulk limit ($N_{\text{layers}} \to \infty$), we recover the volume fraction of spheres in a hexagonal close packed unit cell, $\varphi_{\text{NC, bulk}} = \pi d^3/[3\sqrt{2}(d+s)^3]$.

The above expressions were used to calculate D_{eff} versus N_{layers} using the same values for k_{ligand}, k_{NC}, d, s, and h_c as were used in the finite element simulations stated above. The results appear in Figure 4b. In both cases the volume fraction of the NC core increases with increasing number of SC layers, leading to an increase in k_{eff}. While the averaged volumetric heat capacity ρC_p slightly decreases with increasing number of SC layers, the change in k_{eff} is larger and thus D_{eff} also increases weakly with N_{layers}.

Monte Carlo Simulations: The Monte Carlo simulations of quasi-ballistic transport were programmed in Python version 3.12.3, using a PCG pseudorandom number generator for the scattering angles. The calculations, parallelized with a process pool that handles multiple particles simultaneously, were performed on the supercomputers of Sorbonne Université (MCMeSU). The simulations consist in computing the trajectories of a large number of point-like particles in a two dimensional, two-medium structure composed of a matrix (ligands) filled with a hexagonal array of circles (NCs). In a given medium, the particles travel a distance equal to Λ (mean free path) at a constant speed v before being scattered in a random direction. In the case where the particles reach the edge of a circle (NC–ligand interface) before having traveled a distance Λ since the last scattering event, they have a probability P_t of crossing the boundary and reaching the other medium where their speed and mean free path are updated accordingly and the trajectory is set to a random angle within the second material, or else they are scattered back into the initial material at a random angle. If the particles encounter the ligand–air or ligand–substrate boundary, they are scattered back into the ligand at a random angle. The interfacial scattering points are determined by solving the intersection between a line and a list of circles. The diffusivity is obtained by computing the mean squared displacement from the positions of 10^5–10^6 particles at each time step. In the case of an unconstrained continuous random walk in the Wiener limit, the particle's mean squared displacement is linked to its mean free path and velocity through the relation $\sigma^2 = \Lambda v t$. By using the usual definition of the diffusion coefficient in two dimensions, $\sigma^2 = 4Dt$, we can empirically calculate the velocity needed in the simulation for the carriers to achieve literature values of diffusivity in amorphous PSSH and bulk Au ($v = 4D/\Lambda$). The thermal conductivity, density, heat capacity and mean free path in PSSH were approximated as polystyrene thin films[63] with $k_{PSSH} = 0.15$ W m^{-1} K^{-1}, $\rho_{PSSH} = 1000$ kg m^{-3}, $C_{PSSH} = 1250$ J kg^{-1} K^{-1}, and $\Lambda_{PSSH} = 11.5$ nm,[46] which leads to a diffusivity of $D_{PSSH} = k_{PSSH}/\rho_{PSSH}C_{PSSH} = 120$ nm^2 ns^{-1}. Such diffusivity would be reached for an effective average carrier velocity of $v_{PSSH} = 41.7$ m s^{-1} in two dimensions. For gold, using bulk values of $k_{Au} = 315$ W m^{-1} K^{-1}, $\rho_{Au} = 19{,}320$ kg m^{-3}, $C_{Au} = 129$ J kg^{-1} K^{-1}, and $\Lambda_{Au} = 37.7$ nm,[65] gives an effective velocity of around 13,400 m s^{-1}. We note that the heat carrier velocities are artificially chosen such that plausible literature values are obtained when simulating Au-only or PSSH-only media. While the absolute value of diffusivity depends on the chosen velocity, we ensure that the diffusivity ratio between mono to few-layers and multilayer (D/D_{10L} as shown in Figure 4b-g) is independent of the heat carrier velocity. The probability P_t for phonons to cross an interface in a given material is linked to the interfacial thermal conductance h_c through the equation:[66]

$$P_t = \frac{4h_c}{C_v v + 4h_c}$$

where $C_v = \rho C_p$ is the volumetric heat capacity, and v is typically the sound velocity. While approximate, this single medium model still allows us to gain insight on a plausible range of values for P_t. For C_v and v going from the ligand to the gold values and h_c in the range 50 ± 10 MW m^{-2} K^{-1}, P_t varies from 1% to 5%.

Supporting Information

Supporting Information is available from the Wiley Online Library or from the author.

Acknowledgments

J.K.U. is grateful to Albert Beardo for discussions leading to the notion that straight channels versus curved paths in the ligand matrix may explain the monolayer enhancement. This work was supported by French state funds managed by the Agence Nationale de la Recherche through the grants PV-SCOPE (ANR-24-CE50-5726). This work was supported by the Emergence Research Programme of Alliance Sorbonne Université. M.F. acknowledges the Institute of Materials Science (iMAT) of the Alliance Sorbonne Université for PhD funding.

Conflict of Interest

The authors declare no competing interests.

References

(1) Coates, N. E.; Yee, S. K.; McCulloch, B.; See, K. C.; Majumdar, A.; Segalman, R. A.; Urban, J. J. Effect of Interfacial Properties on Polymer–Nanocrystal Thermoelectric Transport. *Adv. Mater.* **2013**, *25* (11), 1629–1633.

(2) Ibáñez, M.; Luo, Z.; Genç, A.; Piveteau, L.; Ortega, S.; Cadavid, D.; Dobrozhan, O.; Liu, Y.; Nachtegaal, M.; Zebarjadi, M.; Arbiol, J.; Kovalenko, M. V.; Cabot, A. High-Performance Thermoelectric Nanocomposites from Nanocrystal Building Blocks. *Nat. Commun.* **2016**, *7* (1), 10766.

(3) Piotrowski, M.; Franco, M.; Sousa, V.; Rodrigues, J.; Deepak, F. L.; Kakefuda, Y.; Kawamoto, N.; Baba, T.; Owens-Baird, B.; Alpuim, P.; Kovnir, K.; Mori, T.; Kolen'ko, Y. V. Probing of Thermal Transport in 50 Nm Thick PbTe Nanocrystal Films by Time-Domain Thermoreflectance. *J. Phys. Chem. C* **2018**, *122* (48), 27127–27134.

(4) Sousa, V.; Goto, M.; Claro, M. S.; Pyrlin, S.; Marques, L.; Modin, E. B.; Lebedev, O. I.; Alizadeh, S. M.; Freitas, C.; Vieira, E. M. F.; Kovnir, K.; Alpuim, P.; Mori, T.; Kolen'ko, Y. V. PbSe Quantum Dot Superlattice Thin Films for Thermoelectric Applications. *Adv. Funct. Mater.* **2024**, *34* (49), 2409216.

(5) Mueller, N. S.; Okamura, Y.; Vieira, B. G. M.; Juergensen, S.; Lange, H.; Barros, E. B.; Schulz, F.; Reich, S. Deep Strong Light–Matter Coupling in Plasmonic Nanoparticle Crystals. *Nature* **2020**, *583* (7818), 780–784.

(6) Schulz, F.; Lange, H. Optimizing Interparticle Gaps in Large-Scale Gold Nanoparticle Supercrystals for Flexible Light-Matter Coupling. *Adv. Opt. Mater.* **2022**, *10* (24), 2202064.

(7) Liu, M.; Yazdani, N.; Yarema, M.; Jansen, M.; Wood, V.; Sargent, E. H. Colloidal Quantum Dot Electronics. *Nat. Electron.* **2021**, *4* (8), 548–558.

(8) Talapin, D. V.; Lee, J.-S.; Kovalenko, M. V.; Shevchenko, E. V. Prospects of Colloidal Nanocrystals for Electronic and Optoelectronic Applications. *Chem. Rev.* **2010**, *110* (1), 389–458.

(9) Yazdani, N.; Jansen, M.; Bozyigit, D.; Lin, W. M. M.; Volk, S.; Yarema, O.; Yarema, M.; Juranyi, F.; Huber, S. D.; Wood, V. Nanocrystal Superlattices as Phonon-Engineered Solids and Acoustic Metamaterials. *Nat. Commun.* **2019**, *10* (1), 4236.

(10) Lu, B.; Vegso, K.; Micky, S.; Ritz, C.; Bodik, M.; Fedoryshyn, Y. M.; Siffalovic, P.; Stemmer, A. Tunable Subnanometer Gaps in Self-Assembled Monolayer Gold Nanoparticle Superlattices Enabling Strong Plasmonic Field Confinement. *ACS Nano* **2023**, *17* (13), 12774–12787.

(11) Black, C. T.; Murray, C. B.; Sandstrom, R. L.; Sun, S. Spin-Dependent Tunneling in Self-Assembled Cobalt-Nanocrystal Superlattices. *Science* **2000**, *290* (5494), 1131–1134.

(12) Coe, S.; Woo, W.-K.; Bawendi, M.; Bulović, V. Electroluminescence from Single Monolayers of Nanocrystals in Molecular Organic Devices. *Nature* **2002**, *420* (6917), 800–803.

(13) Cavallo, M.; Bossavit, E.; Zhang, H.; Dabard, C.; Dang, T. H.; Khalili, A.; Abadie, C.; Alchaar, R.; Mastrippolito, D.; Prado, Y.; Becerra, L.; Rosticher, M.; Silly, M. G.; Utterback, J. K.; Ithurria, S.; Avila, J.; Pierucci, D.; Lhuillier, E. Mapping the Energy Landscape from a Nanocrystal-Based Field Effect Transistor under Operation Using Nanobeam Photoemission Spectroscopy. *Nano Lett.* **2023**, *23* (4), 1363–1370.

(14) Boong, S. K.; Chong, C.; Lee, J.; Ang, Z. Z.; Li, H.; Lee, H. K. Superlattice-based Plasmonic Catalysis: Concentrating Light at the Nanoscale to Drive Efficient Nitrogen-to-Ammonia Fixation at Ambient Conditions. *Angew. Chem.* **2023**, *135* (7), e202216562.

(15) Herran, M.; Juergensen, S.; Kessens, M.; Hoeing, D.; Köppen, A.; Sousa-Castillo, A.; Parak, W. J.; Lange, H.; Reich, S.; Schulz, F.; Cortés, E. Plasmonic Bimetallic Two-

Dimensional Supercrystals for H2 Generation. *Nat. Catal.* **2023**, *6* (12), 1205–1214.
(16) Xiahou, Y.; Liu, J.; Zheng, J.; Yi, J.; Wang, D.; Xia, H. Performance Improvement of Macroscopical Film of Gold Nanoparticles as Temperature Sensor Derived from Its Mono-Crystallinity. *Chem. Eng. J.* **2023**, *460*, 141835.
(17) Ong, W.-L.; Rupich, S. M.; Talapin, D. V.; McGaughey, A. J. H.; Malen, J. A. Surface Chemistry Mediates Thermal Transport in Three-Dimensional Nanocrystal Arrays. *Nat. Mater.* **2013**, *12* (5), 410–415.
(18) Ong, W.-L.; Majumdar, S.; Malen, J. A.; McGaughey, A. J. H. Coupling of Organic and Inorganic Vibrational States and Their Thermal Transport in Nanocrystal Arrays. *J. Phys. Chem. C* **2014**, *118* (14), 7288–7295.
(19) Liu, M.; Ma, Y.; Wang, R. Y. Modifying Thermal Transport in Colloidal Nanocrystal Solids with Surface Chemistry. *ACS Nano* **2015**, *9* (12), 12079–12087.
(20) Guzelturk, B.; Utterback, J. K.; Coropceanu, I.; Kamysbayev, V.; Janke, E. M.; Zajac, M.; Yazdani, N.; Cotts, B. L.; Park, S.; Sood, A.; Lin, M.-F.; Reid, A. H.; Kozina, M. E.; Shen, X.; Weathersby, S. P.; Wood, V.; Salleo, A.; Wang, X.; Talapin, D. V.; Ginsberg, N. S.; Lindenberg, A. M. Nonequilibrium Thermodynamics of Colloidal Gold Nanocrystals Monitored by Ultrafast Electron Diffraction and Optical Scattering Microscopy. *ACS Nano* **2020**, *14* (4), 4792–4804.
(21) Liang, Y.; Diroll, B. T.; Wong, K.-L.; Harvey, S. M.; Wasielewski, M.; Ong, W.-L.; Schaller, R. D.; Malen, J. A. Differentiating Thermal Conductances at Semiconductor Nanocrystal/Ligand and Ligand/Solvent Interfaces in Colloidal Suspensions. *Nano Lett.* **2023**, *23* (9), 3687–3693.
(22) Wang, Z.; Christodoulides, A. D.; Dai, L.; Zhou, Y.; Dai, R.; Xu, Y.; Nian, Q.; Wang, J.; Malen, J. A.; Wang, R. Y. Nanocrystal Ordering Enhances Thermal Transport and Mechanics in Single-Domain Colloidal Nanocrystal Superlattices. *Nano Lett.* **2022**, *22* (12), 4669–4676.
(23) Utterback, J. K.; Sood, A.; Coropceanu, I.; Guzelturk, B.; Talapin, D. V.; Lindenberg, A. M.; Ginsberg, N. S. Nanoscale Disorder Generates Subdiffusive Heat Transport in Self-Assembled Nanocrystal Films. *Nano Lett.* **2021**, *21* (8), 3540–3547.
(24) Sood, A.; Cheaito, R.; Bai, T.; Kwon, H.; Wang, Y.; Li, C.; Yates, L.; Bougher, T.; Graham, S.; Asheghi, M.; Goorsky, M.; Goodson, K. E. Direct Visualization of Thermal Conductivity Suppression Due to Enhanced Phonon Scattering Near Individual Grain Boundaries. *Nano Lett.* **2018**, *18* (6), 3466–3472.
(25) Feldman, M.; Vernier, C.; Nag, R.; Barrios-Capuchino, J. J.; Royer, S.; Cruguel, H.; Lacaze, E.; Lhuillier, E.; Fournier, D.; Schulz, F.; Hamon, C.; Portalès, H.; Utterback, J. K. Anisotropic Thermal Transport in Tunable Self-Assembled Nanocrystal Supercrystals. *ACS Nano* **2024**, *18* (50), 34341–34352.
(26) Feser, J. P.; Chan, E. M.; Majumdar, A.; Segalman, R. A.; Urban, J. J. Ultralow Thermal Conductivity in Polycrystalline CdSe Thin Films with Controlled Grain Size. *Nano Lett.* **2013**, *13* (5), 2122–2127.
(27) Zanjani, M. B.; Lukes, J. R. Phonon Dispersion and Thermal Conductivity of Nanocrystal Superlattices Using Three-Dimensional Atomistic Models. *J. Appl. Phys.* **2014**, *115* (14), 143515.
(28) Shao, C.; Shiomi, J. Negligible Contribution of Inter-Dot Coherent Modes to Heat Conduction in Quantum-Dot Superlattice. *Mater. Today Phys.* **2022**, *22*, 100601.
(29) Feng, B.; Li, Z.; Zhang, X. Prediction of Size Effect on Thermal Conductivity of Nanoscale Metallic Films. *Thin Solid Films* **2009**, *517* (8), 2803–2807.
(30) Cahill, D. G.; Braun, P. V.; Chen, G.; Clarke, D. R.; Fan, S.; Goodson, K. E.; Keblinski, P.; King, W. P.; Mahan, G. D.; Majumdar, A.; Maris, H. J.; Phillpot, S. R.; Pop, E.; Shi, L. Nanoscale Thermal Transport. II. 2003–2012. *Appl. Phys. Rev.* **2014**, *1* (1), 011305.
(31) Sood, A.; Xiong, F.; Chen, S.; Cheaito, R.; Lian, F.; Asheghi, M.; Cui, Y.; Donadio,

D.; Goodson, K. E.; Pop, E. Quasi-Ballistic Thermal Transport Across MoS_2 Thin Films. *Nano Lett.* **2019**, *19* (4), 2434–2442.
(32) Schulz, F.; Pavelka, O.; Lehmkühler, F.; Westermeier, F.; Okamura, Y.; Mueller, N. S.; Reich, S.; Lange, H. Structural Order in Plasmonic Superlattices. *Nat. Commun.* **2020**, *11* (1), 3821.
(33) Boles, M. A.; Engel, M.; Talapin, D. V. Self-Assembly of Colloidal Nanocrystals: From Intricate Structures to Functional Materials. *Chem. Rev.* **2016**, *116* (18), 11220–11289.
(34) Olson, D. H.; Braun, J. L.; Hopkins, P. E. Spatially Resolved Thermoreflectance Techniques for Thermal Conductivity Measurements from the Nanoscale to the Mesoscale. *J. Appl. Phys.* **2019**, *126* (15), 150901.
(35) Fournier, D.; Marangolo, M.; Fretigny, C. Measurement of Thermal Properties of Bulk Materials and Thin Films by Modulated Thermoreflectance (MTR). *J. Appl. Phys.* **2020**, *128* (24), 241101.
(36) De Bellis, F.; Feldman, M.; Delbono, I.; Royer, S.; Prado, Y.; Cruguel, H.; Lacaze, E.; Lhuillier, E.; Utterback, J. K. Simultaneous Electronic and Thermal Signatures in Pump–Probe Spectroscopy of Semiconductor Nanocrystal Films. *Nano Lett.* **2025**.
(37) Delor, M.; Weaver, H. L.; Yu, Q.; Ginsberg, N. S. Imaging Material Functionality through Three-Dimensional Nanoscale Tracking of Energy Flow. *Nat. Mater.* **2020**, *19* (1), 56–62.
(38) Block, A.; Liebel, M.; Yu, R.; Spector, M.; Sivan, Y.; García de Abajo, F. J.; van Hulst, N. F. Tracking Ultrafast Hot-Electron Diffusion in Space and Time by Ultrafast Thermomodulation Microscopy. *Sci. Adv.* **2019**, *5* (5), eaav8965.
(39) Wang, D.; Koh, Y. R.; Kudyshev, Z. A.; Maize, K.; Kildishev, A. V.; Boltasseva, A.; Shalaev, V. M.; Shakouri, A. Spatial and Temporal Nanoscale Plasmonic Heating Quantified by Thermoreflectance. *Nano Lett.* **2019**, *19* (6), 3796–3803.
(40) Dong, A.; Chen, J.; Vora, P. M.; Kikkawa, J. M.; Murray, C. B. Binary Nanocrystal Superlattice Membranes Self-Assembled at the Liquid–Air Interface. *Nature* **2010**, *466* (7305), 474–477.
(41) Schnedermann, C.; Sung, J.; Pandya, R.; Verma, S. D.; Chen, R. Y. S.; Gauriot, N.; Bretscher, H. M.; Kukura, P.; Rao, A. Ultrafast Tracking of Exciton and Charge Carrier Transport in Optoelectronic Materials on the Nanometer Scale. *J. Phys. Chem. Lett.* **2019**, *10* (21), 6727–6733.
(42) Minutella, E.; Schulz, F.; Lange, H. Excitation-Dependence of Plasmon-Induced Hot Electrons in Gold Nanoparticles. *J. Phys. Chem. Lett.* **2017**, *8* (19), 4925–4929.
(43) Staechelin, Y. U.; Hoeing, D.; Schulz, F.; Lange, H. Size-Dependent Electron–Phonon Coupling in Monocrystalline Gold Nanoparticles. *ACS Photonics* **2021**, *8* (3), 752–757.
(44) Hasselman, D. P. H.; Johnson, L. F. Effective Thermal Conductivity of Composites with Interfacial Thermal Barrier Resistance. *J. Compos. Mater.* **1987**, *21* (6), 508–515.
(45) Cahill, D. G.; Pohl, R. O. Lattice Vibrations and Heat Transport in Crystals and Glasses. *Annu. Rev. Phys. Chem.* **1988**, *39* (1), 93–121.
(46) Feng, T.; He, J.; Rai, A.; Hun, D.; Liu, J.; Shrestha, S. S. Size Effects in the Thermal Conductivity of Amorphous Polymers. *Phys. Rev. Appl.* **2020**, *14* (4), 044023.
(47) Wei, X.; Harazinska, E.; Zhao, Y.; Zhuang, Y.; Hernandez, R. Thermal Transport through Polymer-Linked Gold Nanoparticles. *J. Phys. Chem. C* **2022**, *126* (43), 18511–18519.
(48) Xia, J.; Horst, N.; Guo, H.; Travesset, A. Superlattices of Nanocrystals with Polystyrene Ligands: From the Colloidal to Polymer Limit. *Macromolecules* **2019**, *52* (21), 8056–8066.
(49) Ye, X.; Zhu, C.; Ercius, P.; Raja, S. N.; He, B.; Jones, M. R.; Hauwiller, M. R.; Liu, Y.; Xu, T.; Alivisatos, A. P. Structural Diversity in Binary Superlattices Self-Assembled from Polymer-Grafted Nanocrystals. *Nat. Commun.* **2015**, *6* (1), 10052.

(50) Ritsema Van Eck, G. C.; Chiappisi, L.; De Beer, S. Fundamentals and Applications of Polymer Brushes in Air. *ACS Appl. Polym. Mater.* **2022**, *4* (5), 3062–3087.
(51) Poyser, C. L.; Czerniuk, T.; Akimov, A.; Diroll, B. T.; Gaulding, E. A.; Salasyuk, A. S.; Kent, A. J.; Yakovlev, D. R.; Bayer, M.; Murray, C. B. Coherent Acoustic Phonons in Colloidal Semiconductor Nanocrystal Superlattices. *ACS Nano* **2016**, *10* (1), 1163–1169.
(52) Alajlouni, S.; Beardo, A.; Sendra, L.; Ziabari, A.; Bafaluy, J.; Camacho, J.; Xuan, Y.; Alvarez, F. X.; Shakouri, A. Geometrical Quasi-Ballistic Effects on Thermal Transport in Nanostructured Devices. *Nano Res.* **2021**, *14* (4), 945–952.
(53) McBennett, B.; Beardo, A.; Nelson, E. E.; Abad, B.; Frazer, T. D.; Adak, A.; Esashi, Y.; Li, B.; Kapteyn, H. C.; Murnane, M. M.; Knobloch, J. L. Universal Behavior of Highly Confined Heat Flow in Semiconductor Nanosystems: From Nanomeshes to Metalattices. *Nano Lett.* **2023**, *23* (6), 2129–2136.
(54) Tur-Prats, J.; Gutiérrez-Pérez, M.; Bafaluy, J.; Camacho, J.; Alvarez, F. X.; Beardo, A. Microscopic Origin of Heat Vorticity in Quasi-Ballistic Phonon Transport. *Int. J. Heat Mass Transf.* **2024**, *226*, 125464.
(55) Bui, C. T.; Xie, R.; Zheng, M.; Zhang, Q.; Sow, C. H.; Li, B.; Thong, J. T. L. Diameter-Dependent Thermal Transport in Individual ZnO Nanowires and Its Correlation with Surface Coating and Defects. *Small* **2012**, *8* (5), 738–745.
(56) Feng, X.; Sosa-Vargas, L.; Umadevi, S.; Mori, T.; Shimizu, Y.; Hegmann, T. Discotic Liquid Crystal-Functionalized Gold Nanorods: 2- and 3D Self-Assembly and Macroscopic Alignment as Well as Increased Charge Carrier Mobility in Hexagonal Columnar Liquid Crystal Hosts Affected by Molecular Packing and π-π Interactions. *Adv. Funct. Mater.* **2015**, *25* (8), 1180–1192.
(57) Xu, Z. Heat Transport in Low-Dimensional Materials: A Review and Perspective. *Theor. Appl. Mech. Lett.* **2016**, *6* (3), 113–121.
(58) Mao, J.; Liu, Z.; Ren, Z. Size Effect in Thermoelectric Materials. *Npj Quantum Mater.* **2016**, *1* (1), 16028.
(59) Termentzidis, K.; Chantrenne, P.; Duquesne, J.-Y.; Saci, A. Thermal Conductivity of GaAs/AlAs Superlattices and the Puzzle of Interfaces. *J. Phys. Condens. Matter* **2010**, *22* (47), 475001.
(60) Ghosh, S.; Bao, W.; Nika, D. L.; Subrina, S.; Pokatilov, E. P.; Lau, C. N.; Balandin, A. A. Dimensional Crossover of Thermal Transport in Few-Layer Graphene. *Nat. Mater.* **2010**, *9* (7), 555–558.
(61) Wall, V.; King, S. C.; Kashanchi, G. N.; Li, S.; Li, M.; Galy, T.; Harry, D. I.; Ju, S. E.; Marszewski, M.; Pilon, L.; Hu, Y.; Tolbert, S. H. Understanding the Effect of Nanoparticle Size on Thermal Conductivity in Amorphous Nanoporous Materials Made from Colloidal Building Blocks. *J. Phys. Chem. C* **2022**, *126* (42), 18029–18035.
(62) Zheng, Y.; Zhong, X.; Li, Z.; Xia, Y. Successive, Seed-Mediated Growth for the Synthesis of Single-Crystal Gold Nanospheres with Uniform Diameters Controlled in the Range of 5–150 Nm. *Part. Part. Syst. Charact.* **2014**, *31* (2), 266–273.
(63) Liu, J.; Ju, S.; Ding, Y.; Yang, R. Size Effect on the Thermal Conductivity of Ultrathin Polystyrene Films. *Appl. Phys. Lett.* **2014**, *104* (15), 153110.
(64) Zheng, K.; Sun, F.; Tian, X.; Zhu, J.; Ma, Y.; Tang, D.; Wang, F. Tuning the Interfacial Thermal Conductance between Polystyrene and Sapphire by Controlling the Interfacial Adhesion. *ACS Appl. Mater. Interfaces* **2015**, *7* (42), 23644–23649.
(65) Gall, D. Electron Mean Free Path in Elemental Metals. *J. Appl. Phys.* **2016**, *119* (8), 085101.
(66) Chen, G.; Zeng, T. Nonequilibrium Phonon and Electron Transport in Heterostructures and Superlattices. *Microscale Thermophys. Eng.* **2001**, *5* (2), 71–88.

SUPPORTING INFORMATION
for

Inverted Thickness Dependence of Thermal Transport in Nanocrystal Supercrystals Down to the Monolayer

*Matias Feldman, Juan J. Barrios-Capuchino, Hervé Cruguel, Sébastien Royer, Claire Abadie, Danièle Fournier, Emmanuel Lhuillier, Jose Ordonez-Miranda, Emmanuelle Lacaze, Florian Schulz, James K. Utterback**

M. Feldman, Dr. H. Cruguel, S. Royer, Dr. C. Abadie, Prof. D. Fournier, Dr. E. Lhuillier, Dr. J. Ordonez-Miranda, Dr. E. Lacaze, Dr. J. K. Utterback*

Sorbonne Université, CNRS, Institut des NanoSciences de Paris, 75005 Paris, France

*E-mail: james.utterback@sorbonne-universite.fr

J. J. Barrios-Capuchino, Dr. F. Schulz

Institute for Nanostructure and Solid State Physics, University of Hamburg, Luruper Chaussee 149, 22761 Hamburg, Germany

Table of Contents

I. Electron microscopy images of nanocrystal supercrystals

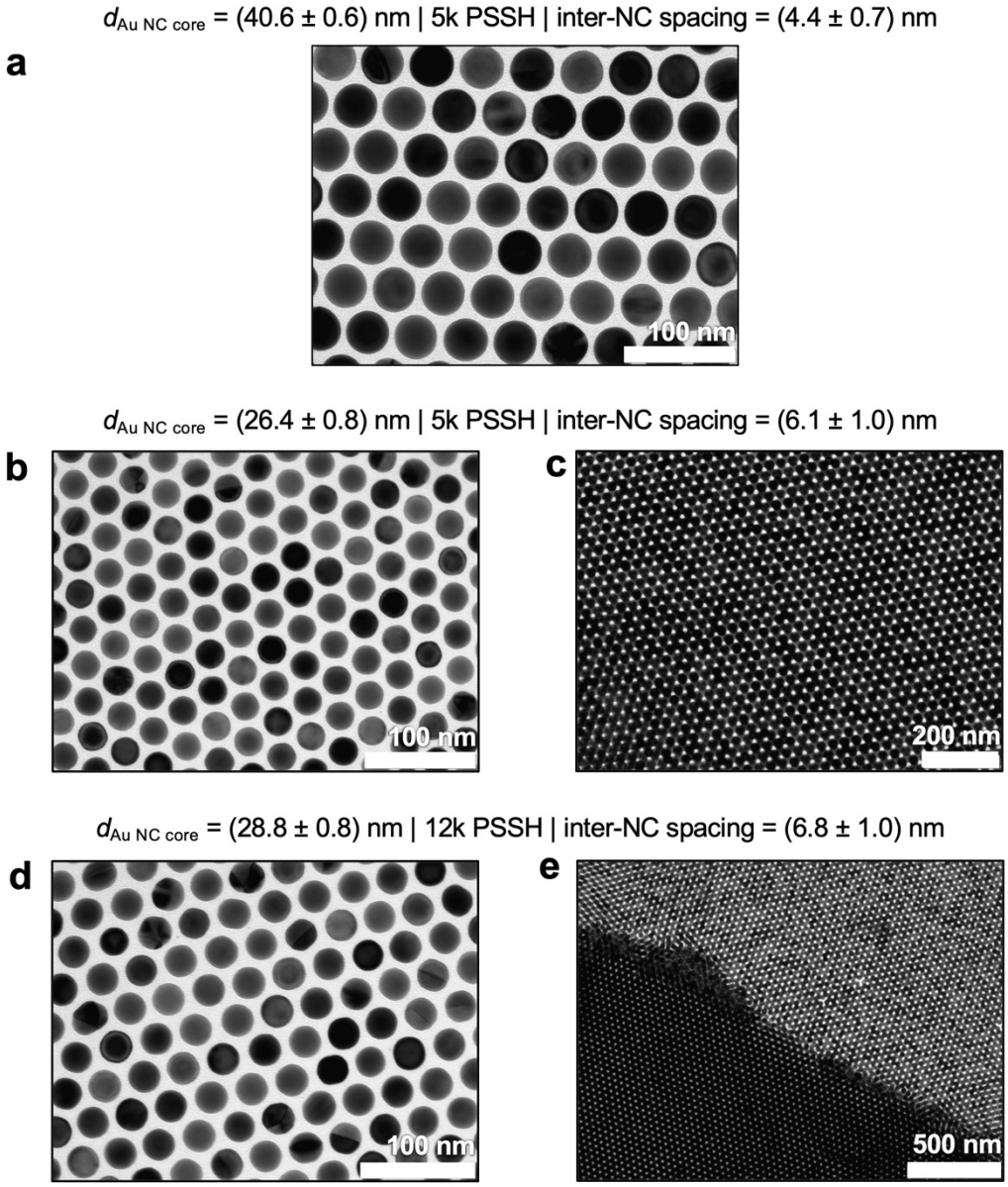

Figure S1. TEM images of Au nanocrystal supercrystals. (a) Monolayer of 40.6 nm nanocrystals with 5k PSSH ligands. (b-c) Monolayer (b) and multilayer (c) of 26.4 nm nanocrystals with 5k PSSH ligands. (d-e) Monolayer (d) and multilayer (e) of 28.8 nm nanocrystals with 12k PSSH ligands.

II. Correlated optical microscopy and AFM

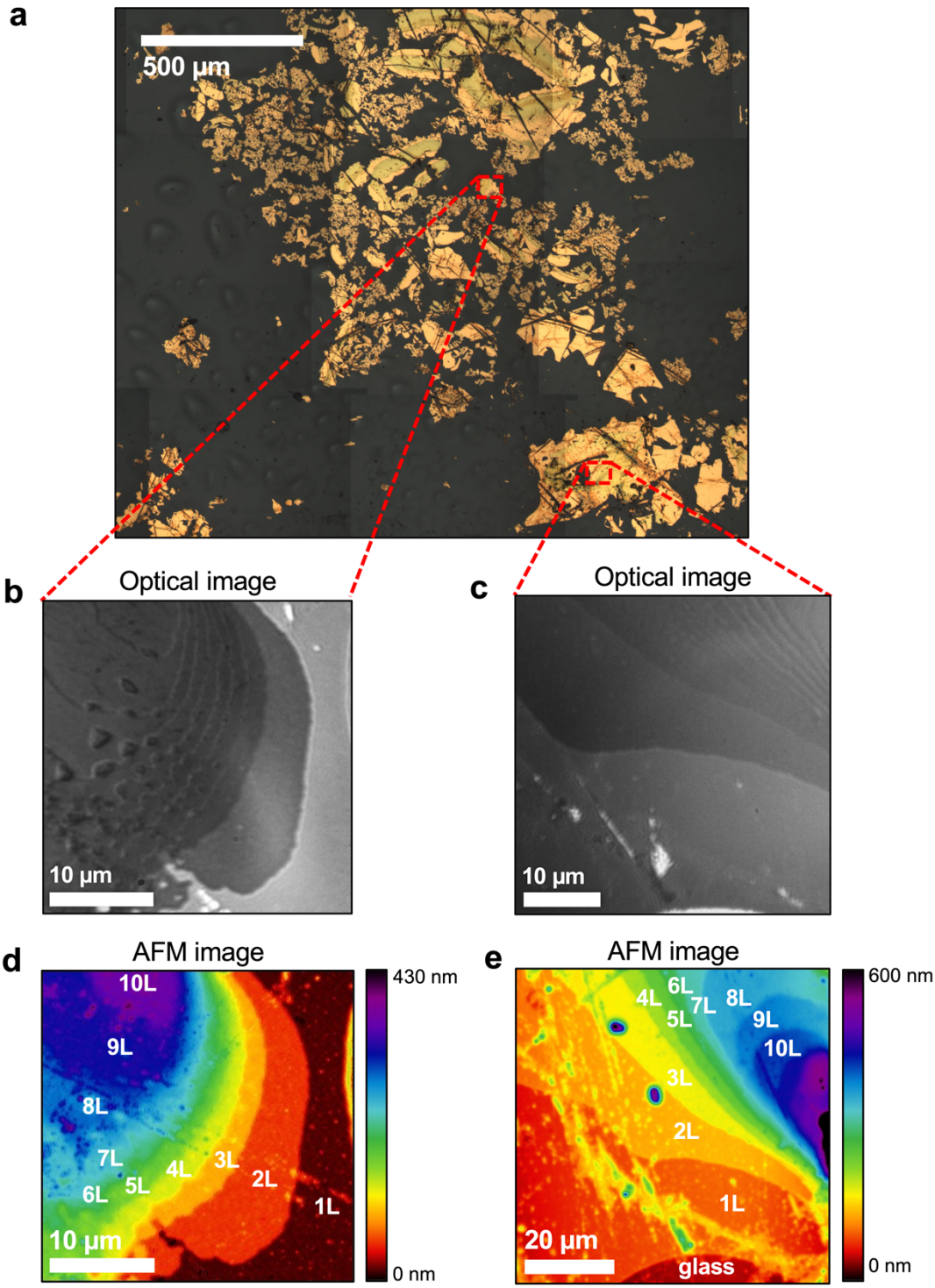

Figure S2. Representative correlated optical and AFM mapping of 40.6 nm Au nanocrystal supercrystal sample. (a) Large area optical reflectance image. Composite image stitched together from several smaller regions. (b,c) Representative regions of interest as imaged in reflectance on spatiotemporally-resolved thermoreflectance microscope, highlighting regions where multiple steps can be seen for N_{layers} = 1–10. (d,e) Topographical AFM images collected for the same regions studied by spatiotemporally-resolved thermoreflectance as pictured in panels (b,c).

III. AFM measurements of supercrystal thickness

Table S1. AFM measurements of nanocrystal supercrystals				
N_{layer}	40.6 nm Au–PSSH5k (4.4 nm gap) Region 1 (Figure S2d)		40.6 nm Au–PSSH5k (4.4 nm gap) Region 2 (Figure S2e)	
	layer thickness (nm)	cumulative thickness (nm)	layer thickness (nm)	cumulative thickness (nm)
1	46.7 ± 0.8	46.7	48.8 ± 1.0	48.8
2	38.3 ± 0.5	85.0	41.1 ± 1.5	89.9
3	37.7 ± 0.5	122.7	39.6 ± 2.0	129.5
4	38.1 ± 0.5	160.8	38.8 ± 0.8	168.3
5	38.0 ± 0.5	198.8	38.8 ± 0.8	207.1
6	38.0 ± 0.5	236.8	39.6 ± 0.8	246.7
7	38.0 ± 0.5	274.8	37.0 ± 1.0	283.7
8	38.0 ± 0.5	312.8	38.7 ± 0.8	321.7
9	38.1 ± 0.8	350.9	37.9 ± 1.0	359.6
10	37.7 ± 0.4	388.6	38.2 ± 0.8	397.8
average for multilayer	38.0 ± 0.5	-	38.8 ± 1.1	-
N_{layer}	26 nm Au–PSSH5k (6.1 nm gap)		29 nm Au–PSSH12k (6.8 nm gap)	
	layer thickness (nm)	cumulative thickness (nm)	layer thickness (nm)	cumulative thickness (nm)
1	31.6 ± 0.6	31.6	42.6 ± 2.3	42.6
2	28.5 ± 0.8	60.1	34.6 ± 1.0	77.2
3	27.8 ± 1.2	87.9	31.5 ± 2.8	108.7
4	28.3 ± 1.2	116.2	30.8 ± 0.3	139.5
5	27.5 ± 0.8	143.7	30.5 ± 1.0	170
average for multilayer	28.0 ± 0.4	-	31.9 ± 1.6	-

All height measurements are given relative to the glass substrate collected in the same AFM image as the series of supercrystal thickness.

AFM measurements were performed in the same regions probed by spatiotemporal thermoreflectance to confirm the local number of supercrystal layers. The thickness as a function of the number of SC layers was measured for all three samples. The results appear in Table S1. We find that the thickness of the monolayer is consistent with the NC diameter (d) plus two times the inter-particle distance (s) measured by TEM. This leads to the assumption in the simulations that the top and bottom ligand layers each have a typical thickness of about $\delta \approx s$ (Figure S4). The thickness of the following layers is consistent with close packing, though with an average layer thickness slightly larger than $(d+s)\sqrt{2/3}$ that would be expected for hard spheres of diameter $d + s$ for the values measured by TEM.

Based on these AFM measurements, we model the SCs as close packed with NC diameters of d and inter-NC spacings of s throughout the middle of the SC, with top and bottom ligand layers of typical thickness $\delta = s$ (Figure S3). This is coherent with a picture in which the ligands highly interdigitate, minimizing the inter-NC spacing. This is the geometry used for our simulations.

For simulations performed in two dimensions, we instead used a vertical spacing of $(d+s)\sqrt{3}/2$ in order to maintain an inter-NC spacing of s as it is a critical parameter for the heat flow between NCs.

We note that the 29 nm Au–PSSH12k is an exception, having an anomalously thick second layer that is 3.7 nm thicker than the average of $N_{\text{layers}} = 3$–5. One explanation for this is that the first and second layers are separated by an extra ligand layer. This could happen for example if, during the self-assembly experiment and likewise during transfer to the substrate from the liquid substrate, already formed monolayers can overlap/stack. This picture is supported by the previous observation of Moiré patterns (Ref 32 of main text). The extra thick bilayer for the 29 nm Au–PSSH12k sample is correlated with a high thermal diffusivity measured for the bilayer for that sample (Figure 3), which qualitatively reinforces the picture that these excess ligand layers act as pathways with reduced scattering that enhance transport.

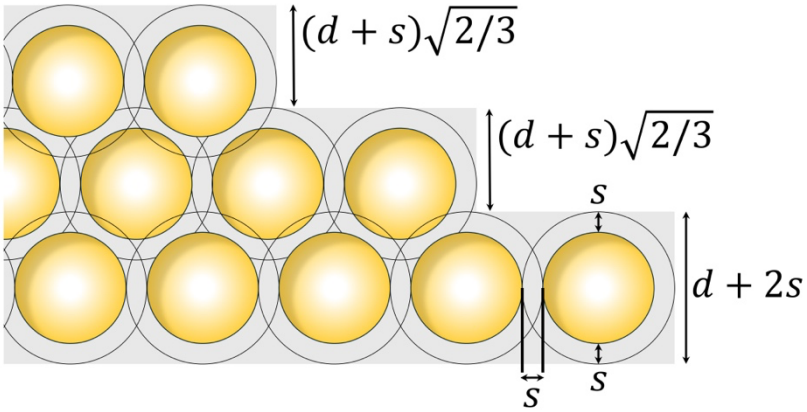

Figure S3. Diagram of three-dimensional hexagonal packing of Au nanocrystals for thicknesses coherent with the AFM data of Table S1. The solid black circles represent a hypothetical ligand shell of thickness s around the nanocrystals. In the hypothesis of high ligand interdigitation between nanocrystals, a top and bottom ligand layer of thicknesses of s naturally arise.

IV. Geometry and temperature profiles from finite element simulations

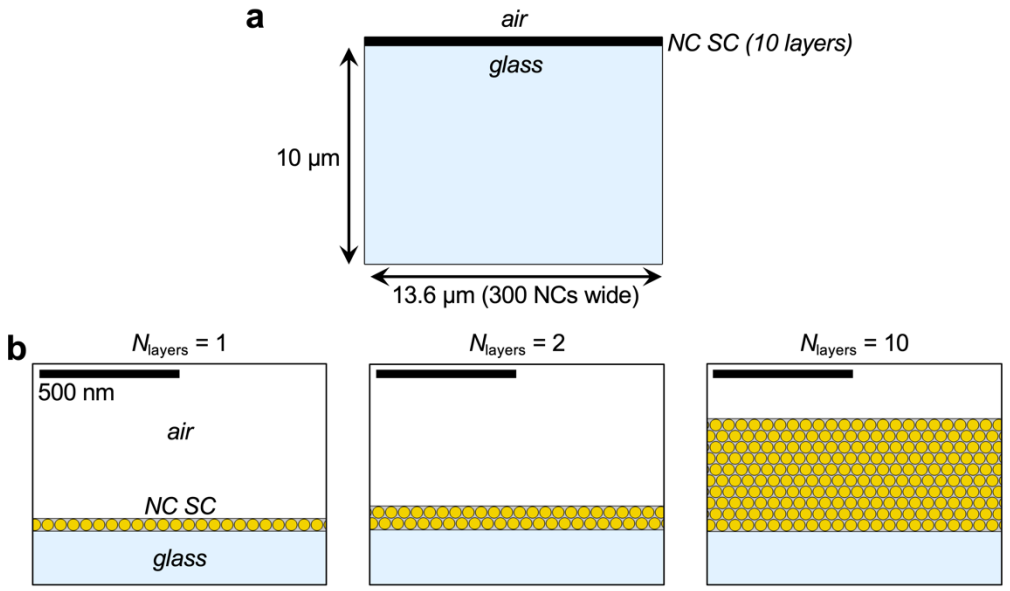

Figure S4. Geometries for finite element simulations with substrate. (a) Full geometry, which was made with a wide enough SC layer (100 to 300 NCs) and thick enough glass substrate to avoid edge effects. (b) Zoom on simulation geometry for hexagonal vertical packing of nanocrystals for N_{layers} = 1, 2, and 10.

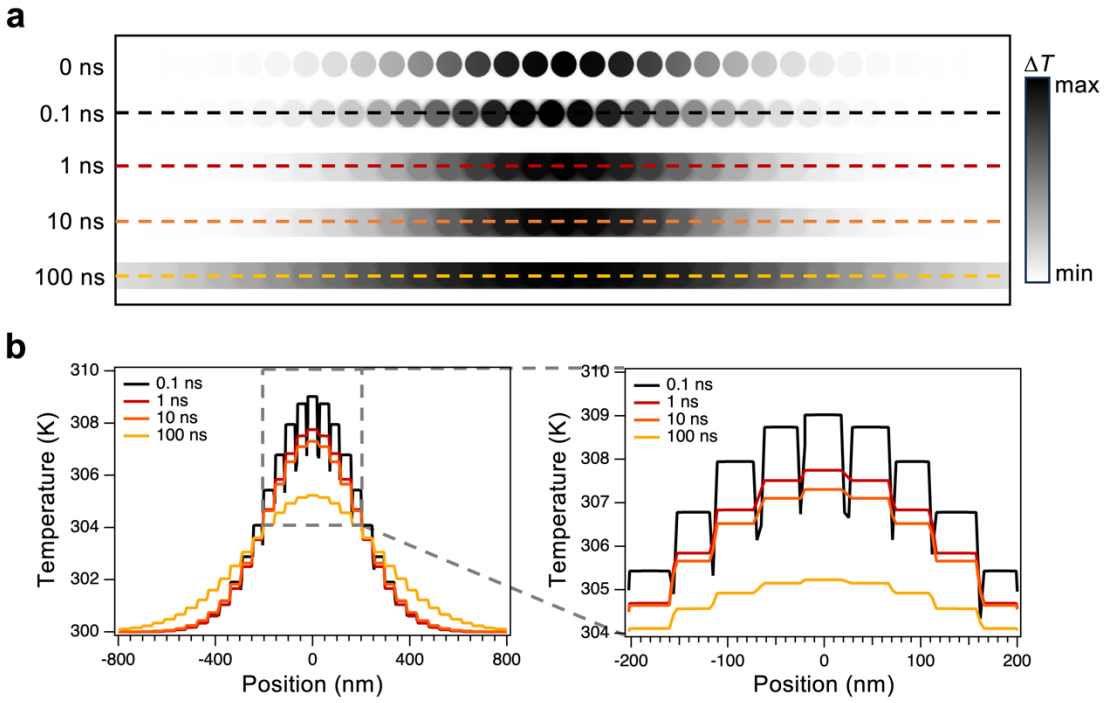

Figure S5. (a) Two-dimensional temperature map and (b) corresponding temperature line cut profiles as a function of time for finite element simulations of a suspended 40.6 nm Au nanocrystal monolayer.

V. Correlated optical microscopy and AFM for suspended monolayer

The suspended monolayer is distinct from the bilayer in that the transition in height is smooth unlike the step-edge observed for transitions between numbers of SC layers. Additionally, the locations interrogated by spatiotemporally-resolved thermoreflectance were lifted 10–20 nm above the flat monolayer—less than a complete monolayer thickness. These points, together with the matching diffusivity for the flat monolayer yet suppression of the late-time acceleration, strongly suggest that the monolayer is lifted from the substrate in this region. This could occur, for example, due to dust underneath the SC nearby or due to strain.

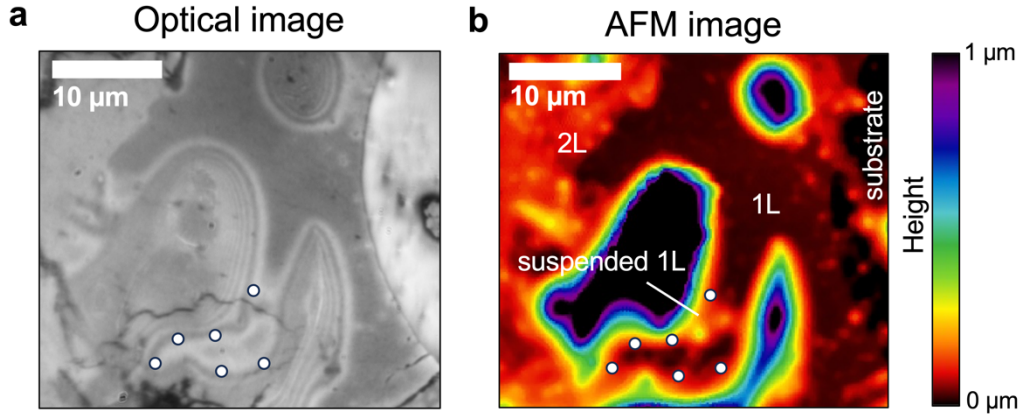

Figure S6. Correlated optical and AFM mapping for a suspended monolayer of 40.6 nm Au nanocrystal supercrystal. (a) Optical reflectance image on spatiotemporally-resolved thermoreflectance microscope and (b) topographical AFM image collected for the same region in which the monolayer is suspended from the substrate. Locations where spatiotemporally-resolved thermoreflectance measurements were performed are indicated as white circles. The average of measurements in these locations is reported in Figure 2.

VI. Mean squared expansion curves for different thicknesses

Figure S7 shows representative experimental and simulated mean squared expansion curves as a function of sample thickness. While the apparent acceleration of heat transport starts around 50 ns in the monolayer, it is delayed to around 100 ns in the bilayer and to >100 ns in the 4-layer SC showcased here. This is consistent with a picture where the late-time acceleration is caused by heat transfer to the glass substrate: the thicker the sample, the longer it takes for the heat to dissipate.

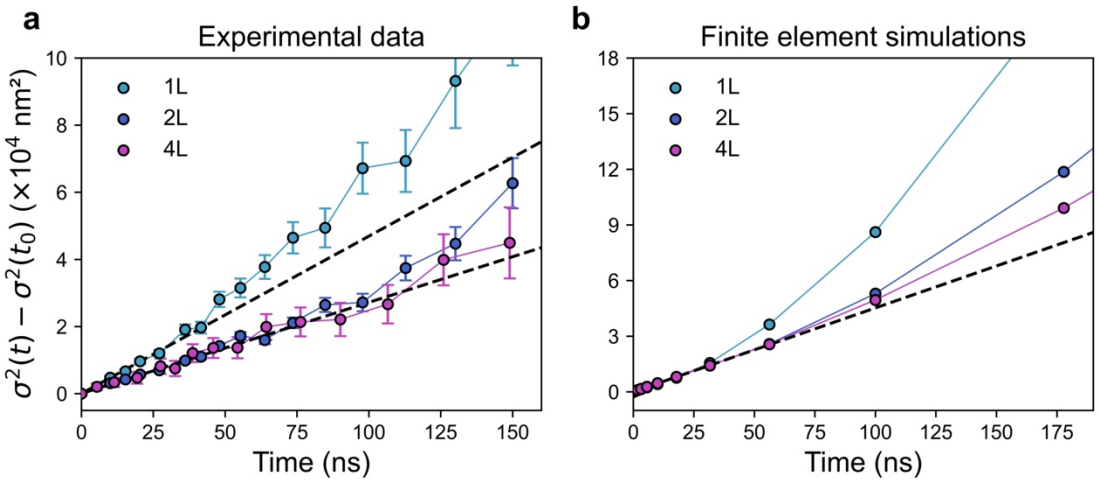

Figure S7. Timescales of heat dissipation to the substrate. Mean squared expansion curves of the transient thermal profile in mono-, bi-, and 4-layers (a) measured in the 41 nm nanocrystal supercrystal and (b) simulated by finite elements for d = 41 nm, s = 4.4 nm, and interfacial thermal conductances of 50 and 5 MW m^{-2} K^{-1} for the NC–ligand and ligand–substrate interfaces, respectively. Black dashed lines in panel (a) are a linear fit to the monolayer and bilayer data in the 10–40 ns time window, and in panel (b) to the monolayer.

VII. EMA in the low interfacial conductance limit

Figure S8 shows the mono-to-ten layer diffusivity ratio versus number of SC layers assuming diffusive thermal transport for different values of the NC–ligand interfacial thermal conductance. In the limit of low interfacial thermal conductance, we obtain an enhancement of the monolayer diffusivity with respect to that of the bulk. This can be understood as an increase in the proportion of highly resistive interfaces that impede thermal transport as more layers are added. In other words, the ligand becomes the dominant conducting medium, and its volume fraction decreases with increasing number of supercrystal layers. However, this behavior becomes relevant only if the interfacial conductance is very small. Specifically, $h_c \approx 2$ MW m^{-2} K^{-1} is required to produce a significant enhancement of about 20%. This value is two orders of magnitude smaller than typical metal–ligand interfacial conductances (100–200 MW m^{-2} K^{-1}) and more than an order of magnitude smaller than the interfacial conductance estimated for our samples (~50 MW m^{-2} K^{-1}). This model is not convincing to explain the behavior in our sample. In contrast, Monte Carlo simulations give a monolayer enhancement of over 20% despite using a more realistic value for h_c by including nanoscale ballistic transport.

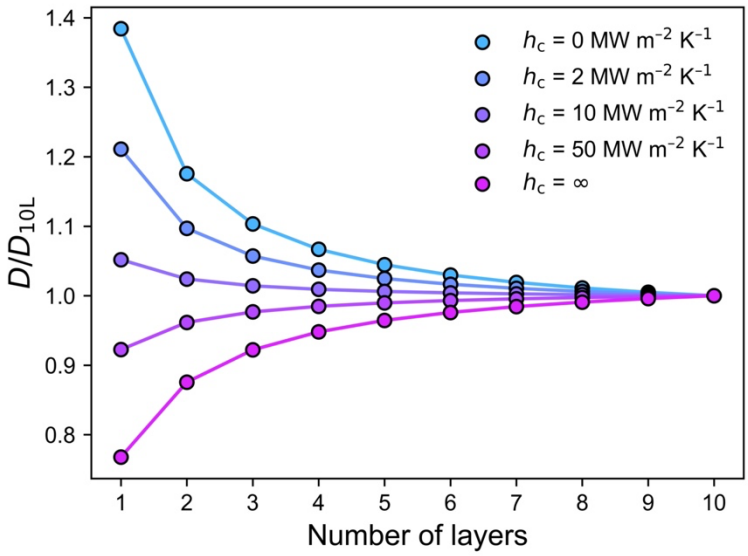

Figure S8. Mono-to-ten layer diffusivity ratios versus number of supercrystal layers predicted by the Hasselman Johnson Maxwell Euken effective medium approximation for different values of NC–ligand interfacial conductance. The geometric and thermal parameters are the same as Figure 4 and appear in the Methods.

VIII. Representative Monte Carlo particle trajectories

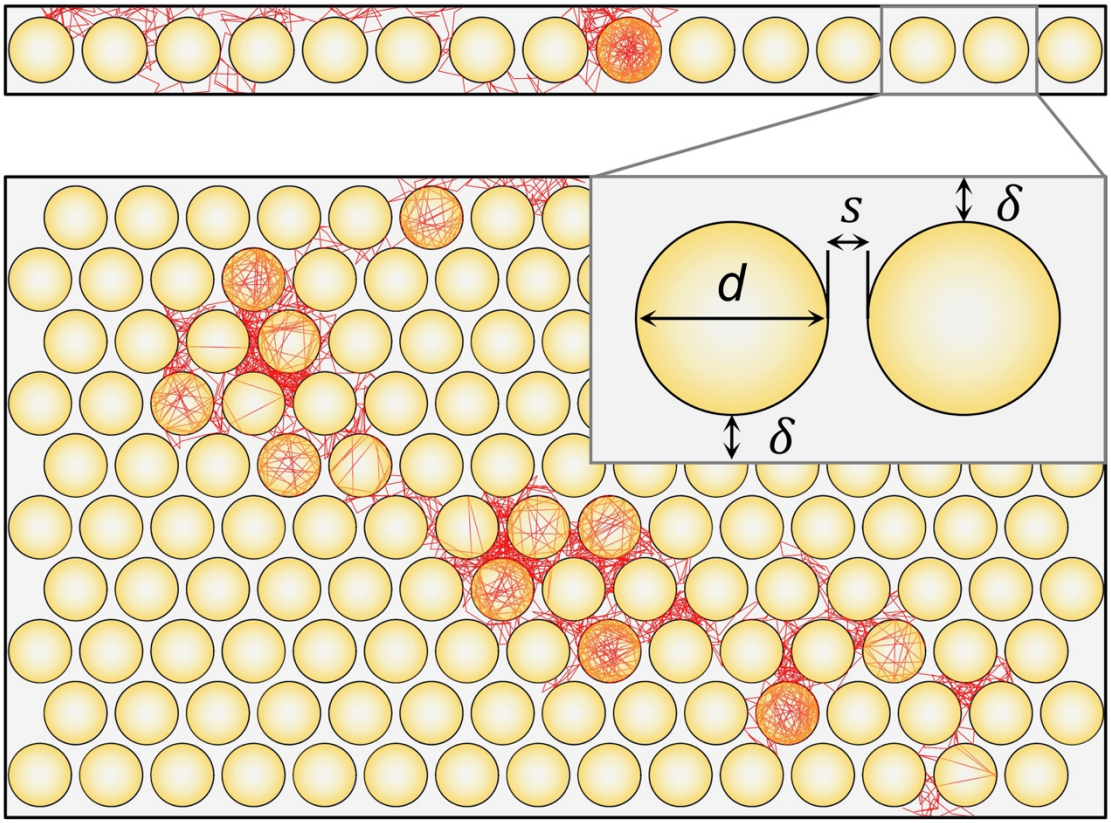

Figure S9. Monte Carlo simulation trajectory of quasi-ballistic thermal transport in mono- and multi-layer nanocrystal supercrystals. Large, zoomed-in version of Figure 4a for visual clarity. Representation of the monolayer and multilayer simulation geometries with example phonon trajectories in red. The inset depicts the definitions of the geometric parameters for the nanocrystal (yellow regions) and ligand (gray regions). The simulations were performed with Λ_{lig} = 11.5 nm, P_t = 1%, d = 30 nm, δ = s = 4 nm, and the material thermal parameters given in the methods.

IX. Quasi-ballistic heat carrier trajectory distribution

It is insightful to examine the distribution of trajectories undertaken by heat carriers in the Monte Carlo simulations of quasi-ballistic transport (Figure 4a). For all particles and all scattering events, we average the distances that are freely traveled after the carriers are scattered at a certain angle θ with respect to the horizontal. Figure S10 shows the distribution of such distances, that is to say the direction-dependent mean free path subject to scattering at interfaces. In the monolayer, the free path distribution is concentrated around $\theta = 0°$ (and 180°) while it is more broad in the multilayer. The 6-fold symmetry of the paths through the interstitial ligand paths in the hexagonal packing dominate for the 10 layer SC. On average, heat carriers travel a longer horizontal or nearly-horizontal distance in the monolayer than in the multilayer. This reveals a preferential direction for heat transport; carriers move more easily horizontally in the monolayer rather than in the multilayer. This enhancement in the free path around $\theta = 0°$ (and 180°) comes from the top and bottom ligand layers of the supercrystal that enable long horizontal paths with fewer scattering centers not available within the bulk.

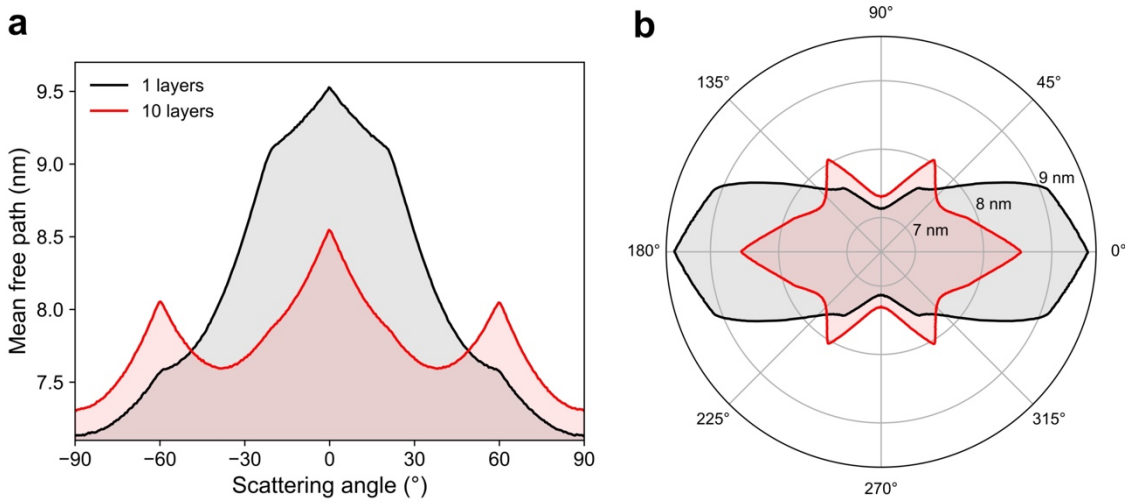

Figure S10. Quasi-ballistic heat carrier trajectories. Distribution (a) and polar plot (b) of heat carrier mean free paths as a function of the scattering angle from Monte Carlo simulations for mono- and multi-layer. The scattering angle is defined relative to the horizontal. Simulations correspond to those in Figure 4. Simulation parameters appear in the Methods.